A Comparison of the Vorticity Dynamics Governing the Oceanic Bomb Cyclone of 4–5 January 1989 and the Super Derecho of 8 May 2009

THOMAS J. GALARNEAU JR.

Cooperative Institute for Mesoscale Meteorological Studies, University of Oklahoma, and NOAA/OAR/National Severe Storms Laboratory, Norman, Oklahoma

MORRIS L. WEISMAN

National Center for Atmospheric Research, Boulder, Colorado

(Manuscript received 11 June 2020, in final form 2 July 2020)

ABSTRACT

Convection-allowing simulations of two warm seclusion cyclones are used to elucidate the vorticity dynamics that contribute to intensification of these systems. The rapidly intensifying oceanic "bomb" cyclone on 4–5 January 1989 and the super derecho on 8 May 2009 are the subject of this study. While these systems occupy different spatial scales, they both acquire characteristics of a warm seclusion cyclone. The aim of this study is to compare the basic structure and determine the dynamics driving increases in system-scale vertical vorticity during the intensification of these systems. Results from a vorticity budget show that system-scale stretching and the lateral transport of vertical vorticity to the cyclone center contribute to increases of system-scale low-level vertical vorticity during the intensification of the oceanic cyclone. The intercomparison of the oceanic cyclone and the super derecho shows that the relative contributions to increases in system-scale vertical vorticity by stretching and tilting as a function of height differ among the two cases. However, the lateral transport of vertical vorticity to the cyclone center is a key contributor to increases in low-level system-scale vertical vorticity for both cases. We hypothesize that this process may be common among a wide array of intense cyclonic systems across scales ranging from warm seclusion extratropical cyclones to some mesoscale convective systems.

1. Introduction

Warm seclusion extratropical cyclones are well known to produce hazardous weather conditions such as flooding rains, heavy snow and blizzard conditions, and damaging winds (Grønås 1995). The warm seclusion process is characterized by the development of a bent-back frontal structure, with a low-level warm core developing separate from the warm sector near the cyclone center (Shapiro and Keyser 1990). Especially strong near-surface winds are often located on the southwest side of the cyclone center (Browning 2004). A similar evolution was documented in association with a warm-season derecho on 8 May 2009 in the midwestern United States (referred to as the super derecho). The super derecho acquired system-scale characteristics that resembled an extratropical cyclone that underwent the seclusion process and developed hurricane-force near-surface winds on the southwest side of the low center (Weisman et al. 2013). A visual comparison of the well-documented oceanic "bomb" cyclone on 4–5 January 1989 sampled by intensive operations period 4 (IOP4) of the Experiment on Rapidly Intensifying Cyclones over the Atlantic (ERICA; Hadlock and Kreitzberg 1988) field program (hereafter referred to as IOP4) and the 8 May 2009 super derecho[1] using visible satellite, radar reflectivity, and estimated positions of the warm and cold fronts shows remarkable similarity

Supplemental information related to this paper is available at the Journals Online website: https://doi.org/10.1175/JAS-D-20-0179.s1.

Corresponding author: Thomas J. Galarneau Jr., tgalarneau@ou.edu

[1] Herein, the term super derecho refers specifically to the intense bookend vortex of the bow-echo mesoscale convective system that was originally named the "super derecho" by Weisman et al. (2013).

DOI: 10.1175/JAS-D-20-0179.1

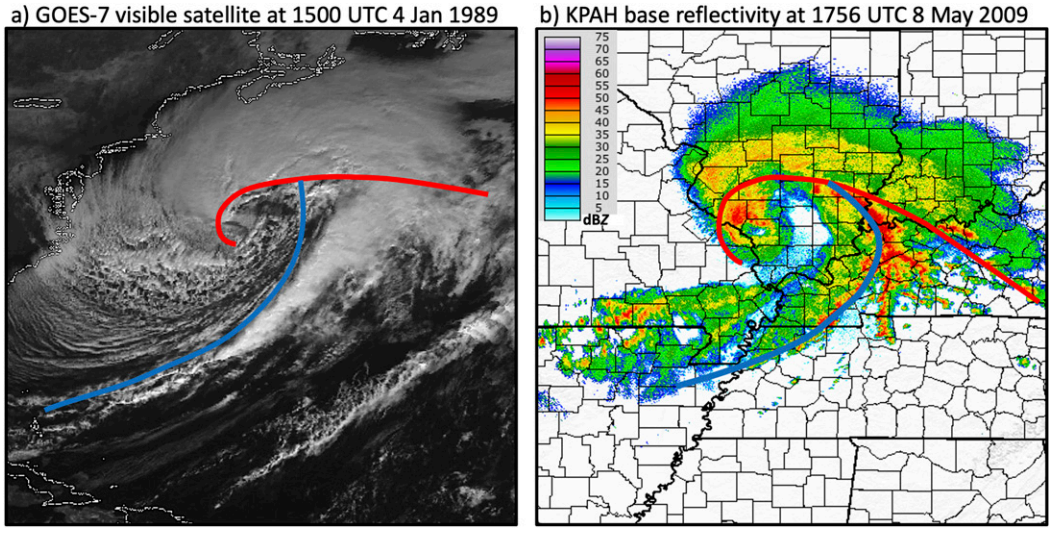

FIG. 1. (a) *GOES-7* visible satellite image at 1500 UTC 4 Jan 1989. Image derived from GridSat B1 data (Knapp et al. 2011). (b) Weather Surveillance Radar-1988 Doppler (WSR-88D) level-II 0.45° base reflectivity (shaded according to the color bar, dB*Z*) from Paducah, Kentucky (KPAH), at 1756 UTC 8 May 2009. Image generated using the NOAA Weather and Climate Toolkit. Estimated positions of warm and cold fronts based on (a) frontal analysis in Neiman and Shapiro (1993, their Fig. 15) and (b) available surface observations and radar imagery and the distribution of 850-hPa equivalent potential temperature in the 3-km ARW simulation, are marked by the red and blue lines, respectively.

in the overall cyclone precipitation, frontal, and warm seclusion structure (Fig. 1). However, the super derecho was not an oceanic extratropical cyclone, rather a long-lived mesoscale convective system, suggesting that the warm seclusion process may not be limited to larger-scale extratropical and some incipient tropical cyclones.

The present paper addresses the development and intensification of two warm seclusion cyclones by comparing convection-allowing (3-km horizontal grid spacing) simulations of IOP4 and the super derecho. These simulations address the following science questions: 1) What are the key mechanisms driving increases in system-scale vertical vorticity during the intensification of the IOP4 and super derecho warm seclusion cyclones? 2) Which features and dynamic processes may be common to the intensification process in both cases despite their different scales and origins?

a. Background on warm seclusion cyclones

Synthesizing the observations collected during ERICA and results from previous numerical modeling studies, Shapiro and Keyser (1990) developed a conceptual model for the life cycle of a warm seclusion cyclone. Herein, we equate Shapiro–Keyser- and warm seclusion–type cyclones. Much like the Norwegian cyclone model (Bjerknes 1919; Bjerknes and Solberg 1922), the Shapiro–Keyser cyclone model begins as a weak perturbation along a baroclinic zone. As the cyclone intensifies, cold and warm fronts rapidly develop. Following the development of fronts, the Shapiro–Keyser model departs from the Norwegian model as the cold front progresses eastward in cyclone-relative space nearly perpendicular to the warm front, and the warm front moves westward in cyclone-relative space and wraps around the cyclone center forming the warm seclusion (Shapiro and Keyser 1990, their Fig. 10.27). On occasion, the beginning and end of Shapiro–Keyser cyclone life cycles can depart from the conceptual model. For example, they can originate from the extratropical transition of tropical cyclones (Harr and Elsberry 2000) prior to the warm seclusion stage or can evolve into tropical cyclones (Davis and Bosart 2003) and tropical cyclone–like systems such as Mediterranean hurricanes and polar lows (Mazza et al. 2017) during the warm seclusion stage.

The development and intensification of warm seclusion cyclones is not only linked to in situ increases in cyclonic vorticity near the storm center, but also the generation of vorticity and potential vorticity (PV) in other regions of the cyclone. In an adiabatic simulation of the IOP4 cyclone, Reed et al. (1994) showed that the warm seclusion cyclone center originated from vorticity that fractured from the southwest end of the bent-back front. Takayabu (1986) showed the evolution of an idealized cyclone in a dry primitive-equation model, illustrating how cyclonic vorticity generated along the occluded front was advected westward to the southwest

end of the occluded front. More recently, Schemm and Wernli (2014) examined warm and cold conveyor belts in idealized Shapiro–Keyser cyclones. The warm conveyor belt is a southerly stream of warm air that occurs within the warm sector of cyclones and is lifted when it reaches the warm and bent-back frontal zones (Carlson 1980). The cold conveyor belt is a low-level easterly stream of cold air north of the warm front that extends from northeast of the cyclone center westward to around the west and south side of the cyclone center. Deep, moist convection occurs most prominently where the warm conveyor belt ascends over the warm and bent-back fronts, resulting in the generation of positive PV in the lower troposphere and negative PV in the upper troposphere. The PV of air parcels embedded in the cold-conveyor-belt airstream increases as they pass through the region where low-level positive PV is being generated in conjunction with latent heating aloft where the warm conveyor belt ascends. The cold-conveyor-belt air parcels transport this higher PV air to the tail of the bent-back front where the formation of an intense low-level jet occurs (Schemm and Wernli 2014).

Clearly, the notion that cyclonic vorticity generated along the warm front and bent-back or occluded fronts is an important characteristic of developing extratropical cyclones has been known for some time. While the results discussed above are derived from idealized numerical experiments, observations from the ERICA field campaign revealed that intense cyclonic circulation centers were common along the warm and bent-back fronts of the Shapiro–Keyser cyclones observed during IOPs 4 and 5 (Neiman and Shapiro 1993; Neiman et al. 1993; Blier and Wakimoto 1995; Wakimoto et al. 1995; Liu et al. 1997). These circulations were associated with convection along the warm and bent-back frontal zones and had horizontal scales of 20–40 km and extended from the surface to 4 km above ground level on average. The circulations were intense, with maximum vorticity values approaching $10^{-2}\,s^{-1}$ (Liu et al. 1997, their Fig. 9). Wakimoto et al. (1995) showed that the center of the IOP5 cyclone originated as one of these intense small-scale circulations. In all, observations support the numerical modeling experiments in that intense cyclonic vorticity features are present along the frontal zones of warm seclusion cyclones. Also, the numerical modeling experiments have suggested that these cyclonic vorticity features are transported westward to near the center of the warm seclusion cyclone.

b. Background on derechos

Derechos are a class of mesoscale convective system that produces extensive swaths of damaging surface winds (e.g., Johns and Hirt 1987; Corfidi et al. 2016). They tend to occur on the anticyclonic side of an upper-level jet and along or slightly north of a low- to midtropospheric warm or stationary front, in an environment characterized by large thermodynamic instability and moderate low-level vertical wind shear (e.g., Evans and Doswell 2001; Coniglio and Stensrud 2004; Guastini and Bosart 2016). Bow-shaped convective systems with strong surface cold pools often represent the dominant mesoconvective structure responsible for the production of the severe winds. Mesoscale circulations such as bookend vortices (e.g., Weisman and Davis 1998) or along-line vortices (e.g., Wakimoto et al. 2006; Atkins and St. Laurent 2009; Wheatley and Trapp 2008; Weisman and Trapp 2003; Trapp and Weisman 2003) are also common features of such systems that can contribute to the production of the severe surface winds and tornadoes. In many cases, the northern bookend vortex will evolve into a balanced mesoscale convective vortex (e.g., Davis and Weisman 1994; Davis and Galarneau 2009), which can impact the development of convection the next day (e.g., Trier and Davis 2007; Galarneau et al. 2009). On more rare occasions, bow echoes can acquire characteristics of a comma-shaped ''mini'' extratropical cyclone (e.g., Fortune et al. 1992; Zhang and Harvey 1995).

The 8 May 2009 super derecho represents perhaps an extreme example of such bow echo to extratropical cyclone evolution. The life cycle, dynamics, predictability, and impacts of this event has been thoroughly documented in the literature (Coniglio et al. 2011, 2012; Weisman et al. 2013; Evans et al. 2014; Grunzke and Evans 2017). The system first developed as a cluster of severe thunderstorms north of a warm front, at the nose of the low-level jet. It quickly organized into a bow-shaped system with a dominant cyclonic mesoscale vortex on its northern end, producing severe surface winds across much of southern Kansas. As the system progressed eastward from southern Kansas into Missouri and Illinois, this northern cyclonic mesoscale vortex intensified into a deep warm-core vortex and the system began to take on visual characteristics of a mesoscale warm seclusion-type cyclone (Fig. 1b).

The convection-allowing Advanced Research Weather Research and Forecasting (ARW; Skamarock et al. 2008) simulations used in this study, and described further in section 2, reveal similarity in the low-level thermal structure and near-surface wind field with a wind maximum located on the southwest side of the surface low pressure center (Fig. 2). The relative maximum in 850-hPa equivalent potential temperature at the center of IOP4 and the super derecho can also be interpreted as a ''moist seclusion,'' in addition to a warm seclusion (Fig. 2). The gust-front region of the super derecho is

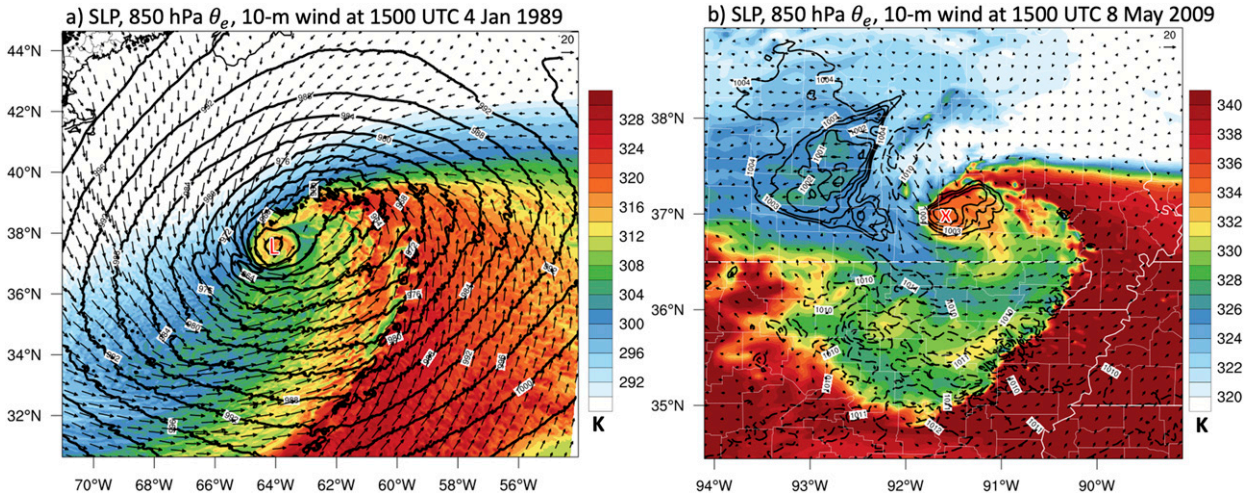

FIG. 2. (a) The 3-km ARW simulated sea level pressure (solid contours every 4 hPa), 10-m wind (arrows, m s^{-1}), and 850-hPa equivalent potential temperature (shaded according to the color bar, K) for IOP4 at 1500 UTC 4 Jan 1989 (15 h). (b) The 3-km ARW simulated sea level pressure (solid contours every 1 hPa for values ≤1004 hPa; dashed contours every 1 hPa for values ≥1010 hPa), 10-m wind (arrows, m s^{-1}), and 850-hPa equivalent potential temperature (shaded according to the color bar, K) for the super derecho at 1500 UTC 8 May 2009 (27 h). The center of IOP4 is marked by a red-filled white "L" and the super derecho by a red-filled white "X."

collocated with a line of thunderstorms and is analogous to the cold front and thunderstorm activity seen with the IOP4 cyclone (Figs. 1 and 2). Also, a warm front extending east from the surface low center is apparent in both systems (Fig. 2). There are also key differences between these two systems beyond the fact that IOP4 is an extratropical cyclone and the super derecho is a mesoscale convective system, namely, that the super derecho has a bubble high and wake low structure ubiquitous to mesoscale convective systems (Fujita 1955) while the IOP4 cyclone does not have these features. Likewise, the IOP4 cyclone occurred on the eastern flank of an intense upper-level trough that underwent cyclonic wave breaking, while the super derecho occurred near a weaker disturbance in the upper troposphere (discussed more in section 3).

c. *Summary of goals and outline*

To address the science questions posed earlier in section 1, we will use a full-physics convection-allowing numerical simulation of the real-data IOP4 case to determine if a similar evolution of cyclonic vorticity occurs during its life cycle as documented in earlier studies of extratropical cyclones (e.g., Takayabu 1986; Reed et al. 1994; Schemm and Wernli 2014). Specifically, we will determine if intense cyclonic vorticity features along the bent-back and warm fronts are transported westward and accumulate in the cyclone center. This analysis will build on previous studies by quantifying the relative role of this lateral transport of vorticity from along the cyclone's fronts in increases of system-scale vorticity of the cyclone.

Given the notable structural similarities in IOP4 and the super derecho, particularly in the low-level thermal structure and wind field, we will use a full-physics convection-allowing numerical simulation of the super derecho to examine the increase of cyclonic vorticity of the warm seclusion center. We will compare these results to the companion analysis of the IOP4 case to determine if a similar evolution of cyclonic vorticity occurs, namely, if the intense cyclonic vorticity features along the gust-front and warm-front region are transported westward and accumulate in the cyclone center similar to the IOP4 case. This analysis will quantify to what extent the vorticity dynamics that spin up the low-level warm seclusion are similar for IOP4 and the super derecho despite their differences in spatial scale.

The remainder of this paper is organized as follows. Section 2 provides a description of the ARW simulations and diagnostic methods used in this study. A comparison of the basic features of IOP4 and the super derecho are shown in section 3. The vorticity budget analysis of IOP4 and the super derecho is presented in section 4. The concluding discussion is presented in section 5.

2. Numerical simulation and vorticity diagnosis

Convection-allowing (3-km horizontal grid spacing) numerical simulations were generated using ARW

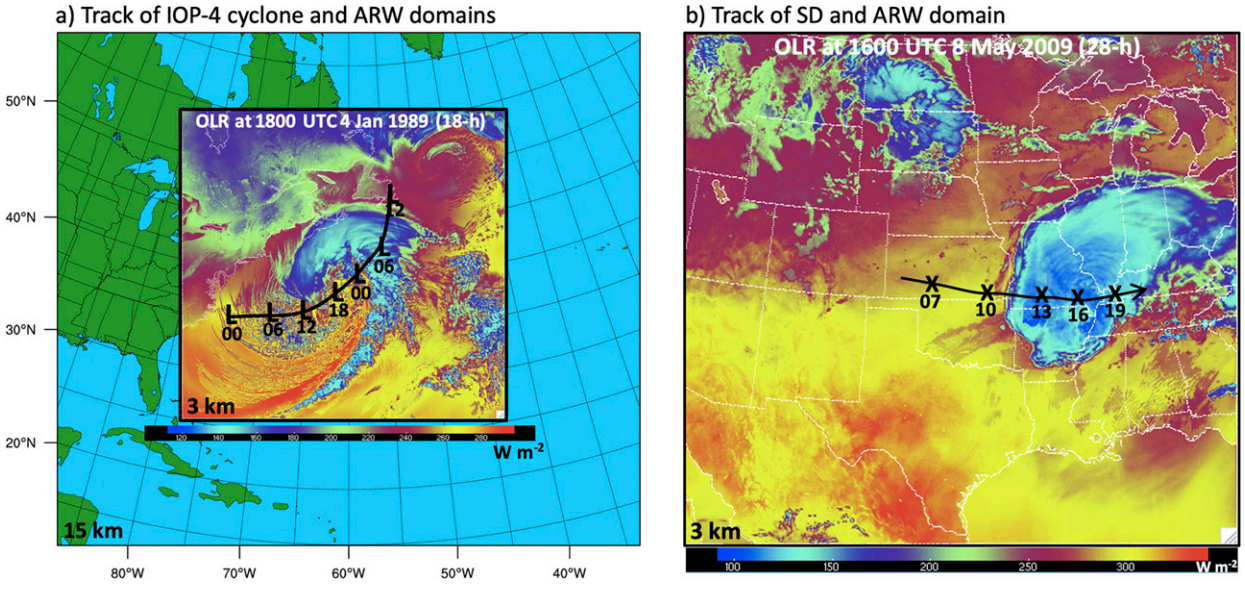

FIG. 3. Geographical locations of ARW model domains for (a) the IOP4 cyclone and (b) the super derecho (SD). In (a), the horizontal grid spacing of the parent domain is 15 km and the inner domain is 3 km. In (b), the horizontal grid spacing of the parent domain is 3 km. On the 3-km domains, outgoing longwave radiation (OLR; shaded according to the color bars, W m^{-2}) and storm tracks are shown. In (a), OLR is shown at 1800 UTC 4 Jan 1989 (18 h) and the storm track is plotted with the thick black line with positions labeled "L" every 6 h. In (b), OLR is shown at 1600 UTC 8 May 2009 (28 h) with the storm track plotted by a thin black line with positions labeled "X" every 3 h. The storm tracks are shown for the extent of the ARW model simulation and the time stamps mark the hour (UTC).

version 3.5.1 for IOP4 and version 3.1 for the super derecho. The model domain configurations are presented in Fig. 3 and the details of the simulation configuration and physics options are summarized in Tables S1 and S2 in the online supplemental material. For IOP4, the 36-h two-way nested simulation was initialized at 0000 UTC 4 January 1989 when the incipient surface cyclone was located near the coast of North Carolina. The physics options are consistent with the "tropical" physics suite available starting with version 3.9 of ARW and have been used previously for hurricane, extratropical transition, and oceanic cyclone applications (e.g., Davis et al. 2008; Galarneau et al. 2013). The 48-h numerical simulation for the super derecho initialized at 1200 UTC 7 May 2009 is the same used by Weisman et al. (2013) and Evans et al. (2014) and used physics options similar to the "CONUS" physics suite available starting with version 3.9 of ARW typically used for real-time convection forecasts in the contiguous United States (Schwartz et al. 2019). The model physical parameterizations are summarized by Evans et al. (2014) and in Table S2.

The evolution of system-scale vertical vorticity for IOP4 and the super derecho is diagnosed using a quasi-Lagrangian vorticity budget. Davis and Galarneau (2009) derived an expression for the time tendency of circulation about a closed region on an isobaric surface as

$$\underbrace{\frac{\partial C}{\partial t}}_{\text{time rate of change of circulation}} = \underbrace{-\overline{\eta}\,\overline{\delta} A}_{\text{stretching}} \underbrace{-\oint \eta' \mathbf{V}' \cdot \hat{\mathbf{n}}\, dl}_{\text{eddy flux}} \underbrace{+\oint \omega \left(\hat{\mathbf{k}} \times \frac{\partial \mathbf{V}}{\partial p} \right) \cdot \hat{\mathbf{n}}\, dl}_{\text{tilting}} \underbrace{+\oint (\hat{\mathbf{k}} \times \mathbf{F}) \cdot \hat{n}\, dl}_{\text{friction}}, \tag{1}$$

where C is the circulation about the closed region, A is the area of the closed region, η is absolute vorticity, δ is divergence, $\mathbf{V}$ is the vector storm-relative wind, p is pressure, $\mathbf{F}$ is the momentum tendency from the planetary boundary layer scheme, l is the unit distance between grid points, $\oint$ represents the line integral around the perimeter of the closed region, and $\hat{\mathbf{n}}$ and $\hat{\mathbf{k}}$ are the unit vectors locally outward normal to the closed region and upward, respectively. Overbars represent the average value around the perimeter of the closed region and primes the local perturbation value relative to the average value around the perimeter of the closed region. The storm-relative wind was computed by subtracting the mean translational velocity of the cyclone center

from the ground-relative wind. The cyclone center was determined by locating the minimum sea level pressure for the IOP4 cyclone and the maximum in 850-hPa relative vorticity for the super derecho.

The forcing terms on the right-hand side of (1) represent mean divergence of mean absolute vorticity around the perimeter of the closed region (i.e., stretching), transport of perturbation absolute vorticity by the perturbation wind across the perimeter of the closed region (i.e., horizontal advection, or eddy flux), tilting of horizontal vorticity by vertical velocity along the perimeter of the closed region, and frictional dissipation about the perimeter of the closed region. A detailed description and interpretation of the third term (tilting of horizontal vorticity) is provided by Davis and Galarneau (2009, their section 2b). Utilizing the relationship between circulation and vertical vorticity, $\zeta = C/A$, the tendency of circulation and the relative contributions for each term will be presented as a vertical vorticity tendency.

The scale of the closed region, or box, used for the vertical vorticity budget was 240 km × 240 km for IOP4 and 90 km × 90 km for the super derecho centered on the cyclones. The size of the closed region was chosen to encompass the entire low-level warm seclusion with the box edges approximately collocated with the radius of maximum wind at 850 hPa. The size of the closed region for the super derecho is consistent with Evans et al. (2014), who used a 100 km × 100 km region in a similar implementation of (1). To account for uncertainties in the location of the cyclone center, we used the vorticity budget ensemble approach used by Davis and Galarneau (2009) and others, where the closed region was shifted from its central location by ±45 km in 3-km increments in the x and y directions, resulting in a 961-member budget ensemble at each time for the convection-allowing simulation of IOP4. Shifting of the closed region by ±30 km in 3-km increments (441-member budget ensemble) was used for the convection-allowing simulation of the super derecho. The results presented herein are derived from the ensemble mean vorticity budget. The value of using the vorticity budget method described above is that we can quantify how convective-scale vorticity features located away from the cyclone center contribute to changes in net vertical vorticity as they merge with the primary cyclone center. Several recent papers have similarly used this vorticity budget method to study the vorticity dynamics of cyclonic disturbances such as mesoscale convective vortices (e.g., Davis and Galarneau 2009; Clark et al. 2010), bookend vortices (e.g., Evans et al. 2014), tropical cyclones (e.g., Rios-Berrios et al. 2016a,b, 2018), and cyclones undergoing extratropical transition (e.g., Galarneau et al. 2013).

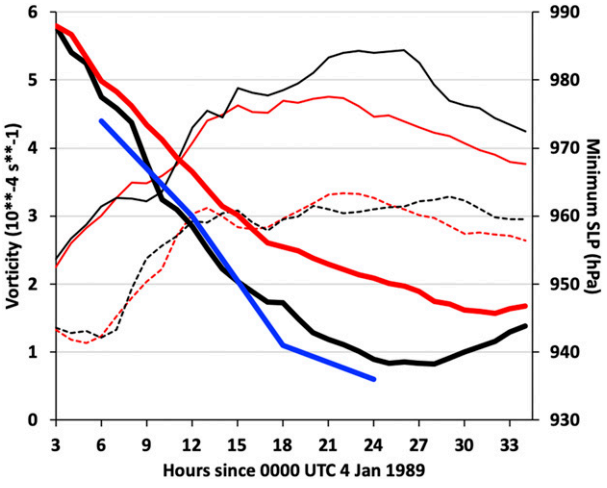

FIG. 4. Time series of minimum sea level pressure (hPa; right y axis) for IOP4 in observations [thick solid blue line; based on Neiman and Shapiro (1993, their Fig. 3)], 3-km ARW (thick solid black line), and 15-km ARW (thick solid red line). Also shown is the area-mean vertical vorticity (10^{-4} s^{-1}; left y axis) in a 240 km × 240 km region centered on the cyclone center for the 3-km ARW at 850 (thin solid black line) and 500 hPa (black dashed line) and 15-km ARW at 850 (thin solid red line) and 500 hPa (dashed red line). Results from the 15-km ARW simulation are provided in the online supplemental material.

3. Comparison of IOP4 and the super derecho

a. IOP4 life cycle

The IOP4 cyclone began as a low pressure system along the North Carolina coastline at 0000 UTC 4 January 1989 with a minimum sea level pressure of 996 hPa (not shown). By 0000 UTC 5 January, the IOP4 cyclone had undergone significant deepening as the minimum sea level pressure decreased to 936 hPa (Neiman and Shapiro 1993), thus qualifying as a meteorological "bomb" cyclone based on the definition by Sanders and Gyakum (1980). The time series of minimum sea level pressure shows that the 3-km ARW simulation was able to reproduce the observed rapid deepening of IOP4, reaching 938 hPa by 0000 UTC 5 January (Fig. 4). Deepening rates were highest at 0300–1500 UTC 4 January, reaching approximately −3.3 hPa h^{-1} [$\sim$−80 hPa (24 h)$^{-1}$] in both the 3-km ARW simulation and observations.

The rapid deepening of IOP4 occurred on the eastern flank of an upper-level trough that moved east from over the northeast United States to the western North Atlantic. The upper-level trough is marked by high-PV stratospheric air with PV values at 250 hPa exceeding 8 PV units (PVU; 1.0 PVU = 1.0 × 10^{-6} K kg^{-1} m^2 s^{-1}) (Fig. 5a). The developing IOP4 cyclone moved eastward initially through 0600 UTC 4 January as it was embedded

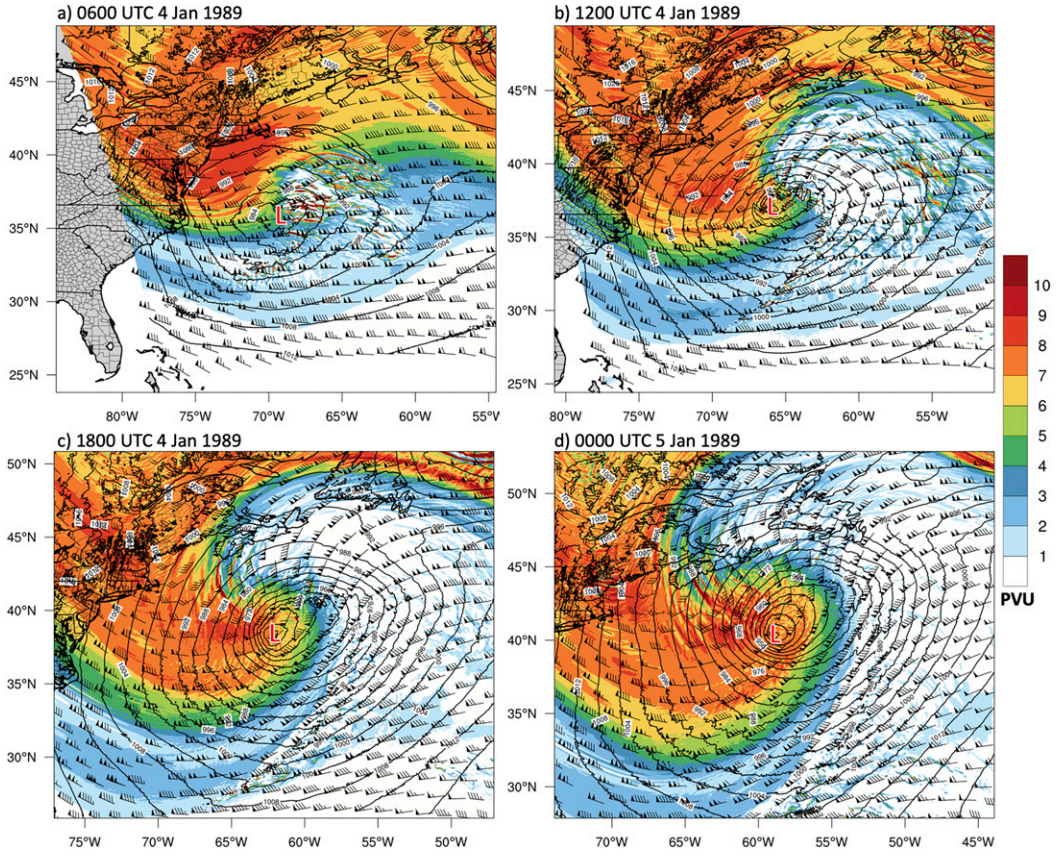

FIG. 5. The 3-km ARW simulated PV (shaded according to the color bar, PVU), wind (half barb = 2.5 m s^{-1}; full barb = 5.0 m s^{-1}; pennant = 25.0 m s^{-1}) and sea level pressure (solid contours every 4 hPa) at (a) 0600 UTC 4 Jan (6 h), (b) 1200 UTC 4 Jan (12 h), (c) 1800 UTC 4 Jan (18 h), and (d) 0000 UTC 5 Jan 1989 (24 h). The center of IOP4 is marked by a red-filled white "L."

in strong westerly flow associated with the upper-level trough located farther west. Cyclonic wave breaking (Thorncroft et al. 1993) was readily underway by 1200 UTC 4 January and was further accentuated by robust ridge-building north and northeast of IOP4 through 0000 UTC 5 January (Figs. 5b–d). As the ridge at 250 hPa developed north of the surface low and the upper-level trough wrapped cyclonically around the south side of the surface low, IOP4 was steered on a northeasterly course toward Newfoundland and Labrador, Canada.

At low levels, IOP4 was in the early stages of its life cycle at 0600 UTC 4 January with well-defined warm and cold fronts and a warm sector still connected to the cyclone center (Fig. 6a). As IOP4 rapidly deepened, the warm front extended westward and wrapped cyclonically around the cyclone center as a bent-back front and the cold front moved eastward relative to the cyclone center by 1800 UTC 4 January (Figs. 6b,c). The strongest near-surface winds exceeding 40 m s^{-1} were located on the southwest side of the cyclone center. By 0000 UTC 5 January, the center of IOP4 was enveloped in a warm region and the warm sector was fully separated from the cyclone center (Fig. 6d).

From the vorticity perspective, the rapid deepening of IOP4 was concurrent with marked increases in area-mean vertical vorticity at 850 and 500 hPa in a 240 km × 240 km region centered on the cyclone during 0300–1500 UTC 4 January (Fig. 4). The marked increases in system-scale vertical vorticity motivates the use of a vorticity budget to determine the processes that led to these increases. For comparison, the time series of minimum sea level pressure and area-mean vertical vorticity for a convection-parameterizing 15-km ARW simulation of IOP4 is also shown. Both simulations similarly represent the rapid deepening of IOP4, although the 3-km ARW simulation showed higher increases in vertical vorticity at 850 hPa after 1500 UTC. Because of the similar increases in vertical vorticity during the rapid intensification period (0300–1500 UTC) in the two simulations, a vorticity budget analysis for the 15-km ARW simulation is provided in the online

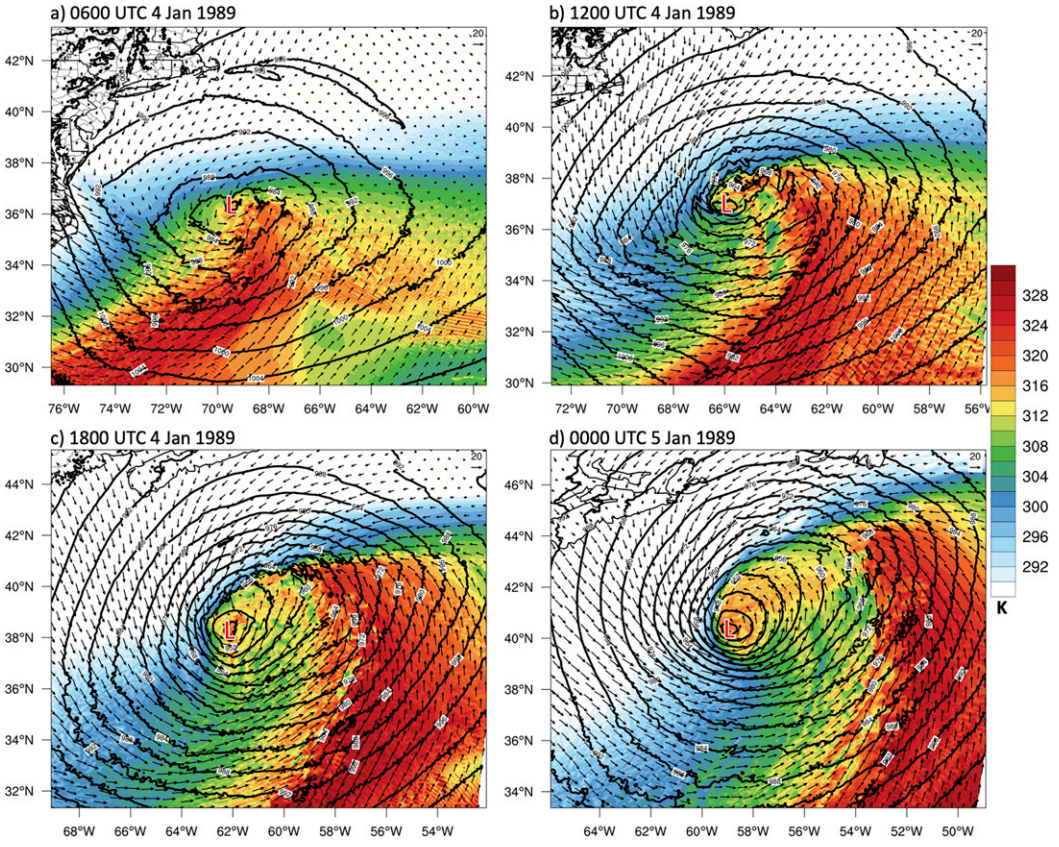

FIG. 6. As in Fig. 2a, but at (a) 0600 UTC 4 Jan (6 h), (b) 1200 UTC 4 Jan (12 h), (c) 1800 UTC 4 Jan (18 h), and (d) 0000 UTC 5 Jan 1989 (24 h). The center of IOP4 is marked by a red-filled white "L."

supplemental material to compare and contrast the processes that led to these increases in the two simulations.

b. *Super derecho life cycle*

The life cycle of the super derecho has been reviewed extensively in observations (Coniglio et al. 2011, 2012) and in the 3-km ARW simulation used herein (Weisman et al. 2013; Evans et al. 2014). A brief overview is provided here. The super derecho began as a cluster of thunderstorms located in southwest Kansas early on 8 May 2009, and by 0600 UTC was located on the north side of a synoptic-scale low pressure system in the southern plains and beneath the poleward exit region of an upper-level jet (not shown). The upper-level jet was associated with a weak trough, marked as a region of positive PV at 250 hPa (not shown). By 0900 and 1200 UTC, the super derecho had evolved into a bow echo with an intense bookend vortex and moved east to southwest Missouri (Weisman et al. 2013, their Fig. 2). By 1500 UTC 8 May, the super derecho was located in south-central Missouri and had remained in the left exit region of the upper-level jet as it moved east away from the surface low pressure system (Fig. 7). The bulk upscale effects of latent heating helped to build a large negative PV anomaly at 250 hPa north and northeast of the super derecho.

The structure of the super derecho at low levels evolved rapidly after 1200 UTC 8 May as it moved through southern Missouri. At 1200 UTC 8 May, the intense bookend vortex was still connected to the warm sector ahead of the gust front (Fig. 8a and Fig. S1a). After 1200 UTC, however, the cold pool gust front moved eastward away from the bookend vortex, eventually completely separating the low-level warm core of the bookend vortex from the high equivalent potential temperature air in the prestorm environment by 1700 UTC (Figs. 8b–f and Figs. S1b–f). By 1500 UTC 8 May, the sea level pressure, near-surface wind, and 850-hPa equivalent potential temperature distribution resembled a synoptic-scale warm seclusion cyclone, except on a smaller scale (Fig. 8d). The meridional temperature gradient that extended east from the super derecho served as the warm front and the cold pool gust front as the cold front. The bookend vortex has a warm seclusion structure, with the strongest low-level

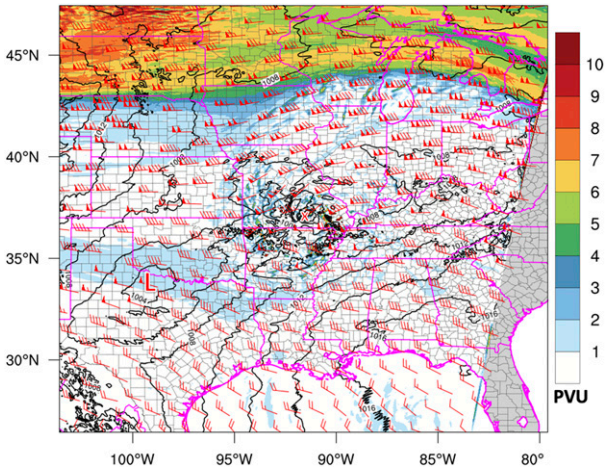

FIG. 7. The 3-km ARW simulated 250-hPa PV (shaded according to the color bar, PVU), wind (barbs as in Fig. 5), and sea level pressure (black contours every 2 hPa) at 1500 UTC 8 May 2009 (27 h). The center of the super derecho mesovortex is marked by a red-filled white "X." Synoptic-scale lee trough is marked by a red-filled white "L."

winds located on the southwest side of the low pressure center.

The time series of area-mean vertical vorticity in a 90 km × 90 km region centered on the cyclone center shows that the bookend vortex was most intense at 1330 UTC 8 May (25.5 h), with vertical vorticity values near $8 \times 10^{-4}\,s^{-1}$ at 700 and 850 hPa (Fig. 9a). As the bookend vortex weakened thereafter and the structure evolved to a warm seclusion, there was a brief reinvigoration of the system-scale vertical vorticity at 900 and 850 hPa between 1500 and 1600 UTC (Fig. 9a and Figs. S1d,e). Hurricane-force near-surface winds occurred on the southwest side of the cyclone center during the reinvigoration (Figs. 8d,e; see also Weisman et al. 2013, their Fig. 7h), while intense convection remained near the cyclone center and the leading convective line moved eastward (Fig. 9b).

c. *Comparison of basic features and structures*

The similar visual characteristics of IOP4 and the super derecho in the satellite and radar imagery was also represented in the 3-km ARW simulations (cf. Figs. 1 and 2). Both systems acquired a warm seclusion cyclone center with a near surface wind maximum on its southwest side with similar positions of bent-back, warm, and cold fronts if the cold pool gust-front boundary in the super derecho is considered the mesoscale analogy to a true synoptic-scale cold front. The remarkable similar structure with these two systems occurred despite the marked differences in synoptic-scale flow, with IOP4 evolving in conjunction with cyclonic wave breaking and the super derecho located near a relatively weaker upper-level disturbance (Figs. 5 and 7). The vertical structure of the warm seclusion cyclone center shows a deep warm core structure extending from near the surface to at least 400 hPa for both systems (Fig. 10). An ascent–descent couplet is located near the west side of the warm seclusion for both systems. Key differences in structure include a region of well-mixed warm air in the 800–600-hPa-layer 80–120 km west of the super derecho center that represents a warm anomaly associated with a descending rear-inflow jet, and a well-mixed boundary layer in IOP4 (Fig. 10).

Storm-relative backward air-parcel trajectories[2] seeded at 850 hPa near the cyclone center shows that air originates both at higher altitudes west of the cyclone center and at low altitudes east of the cyclone center for IOP4 (Fig. 11a). The trajectories that originate west of the cyclone center descend by 200 hPa as they approach the cyclone center, while trajectories that originate to the east are located north of the warm front below 900 hPa and are likely associated with the cold-conveyor-belt airstream and ascend as they approach the cyclone center (Figs. 11a,b). Both streams of air parcels undergo increases in relative vorticity as they approach the cyclone center, with air parcels originating from the east having larger increases in relative vorticity. The super derecho has similar airstreams represented by storm-relative trajectories, with source regions at higher altitudes west of the cyclone center and at lower altitudes east of the cyclone center (Fig. 11c). The trajectories from the east are mostly located north of the warm front similar to IOP4, except that they are located at slightly higher altitudes (Fig. 11d). Similar to IOP4, air parcels in both airstreams undergo increases in relative vorticity, with air parcels originating from the east having larger increases in relative vorticity.

In all, despite the differences in origin and the synoptic-scale flow in which these two systems occurred, their system-scale structure was remarkably similar. The key similarities include the presence of a well-defined warm seclusion, frontal structure, near-surface wind maximum, and storm-relative airstreams. Given the similarities of these two systems, inspection of the physical processes that are linked to their intensification will be explored.

[2] Air-parcel trajectories were computed using the Read/Interpolate/Plot software package (http://www2.mmm.ucar.edu/wrf/users/docs/ripug.htm) by linearly interpolating 10-min velocity data to a 100-s trajectory time step for IOP4 and 5-min velocity data to a 50-s trajectory time step for the super derecho.

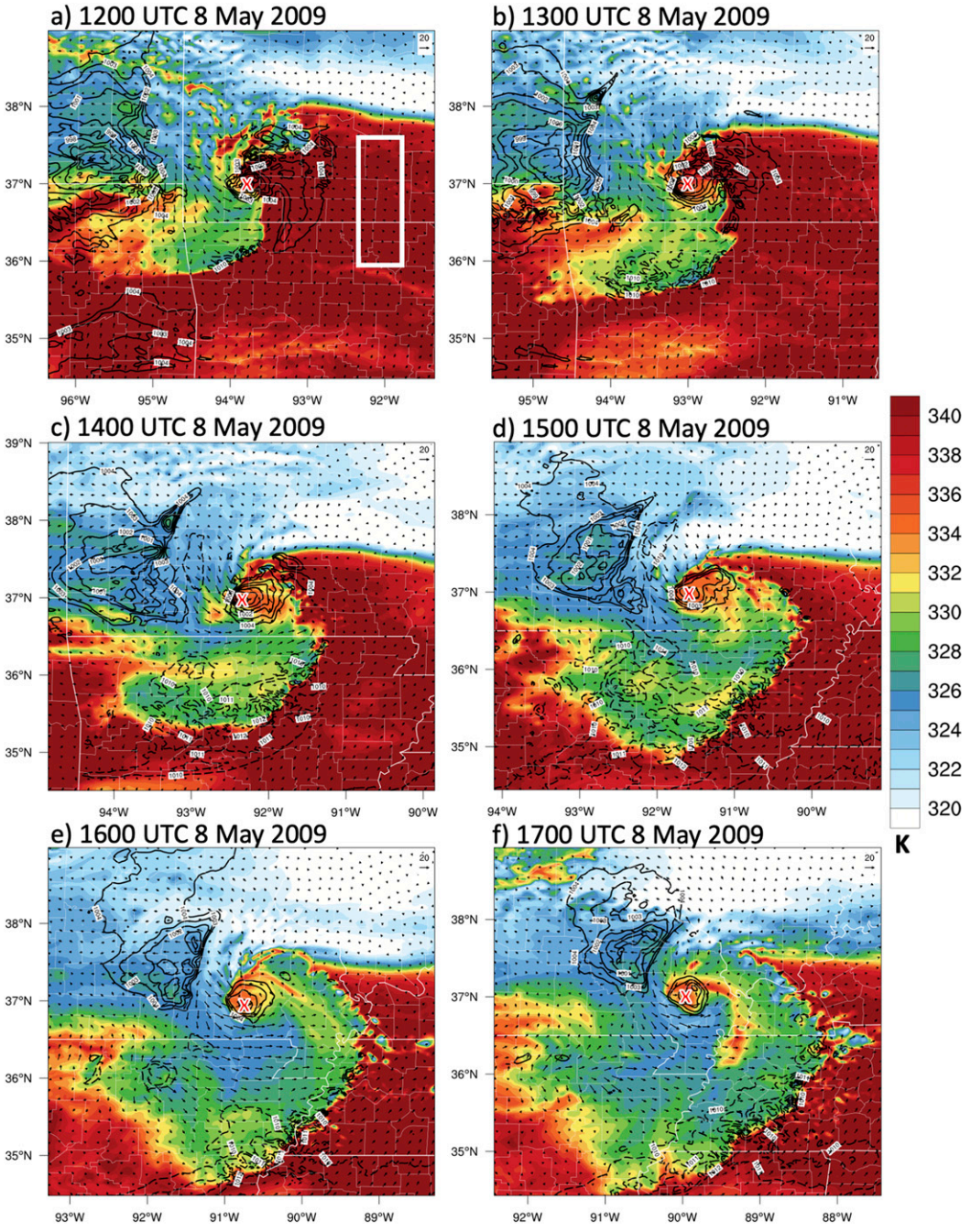

FIG. 8. As in Fig. 2b, but for (a) 1200 (24 h), (b) 1300 (25 h), (c) 1400 (26 h), (d) 1500 (27 h), (e) 1600 (28 h), and (f) 1700 UTC 8 May 2009 (29 h). The center of the super derecho mesovortex is marked by a red-filled white "X." The area-averaging region for Fig. S5 is shown with a white box in (a).

4. Vertical vorticity budget

a. IOP4

The vorticity budget for IOP4 was generated by computing the terms in (1) from the hourly ARW output files. The terms were then multiplied by 3600 s to convert an instantaneous vertical vorticity tendency with units of s^{-2} to an hourly change in vorticity with units of $s^{-1}\,h^{-1}$. Comparison of the budget terms to the actual vertical vorticity change was done by adding the hourly vorticity tendencies for each term on the right-hand side of (1) and comparing that to the actual vorticity change for a

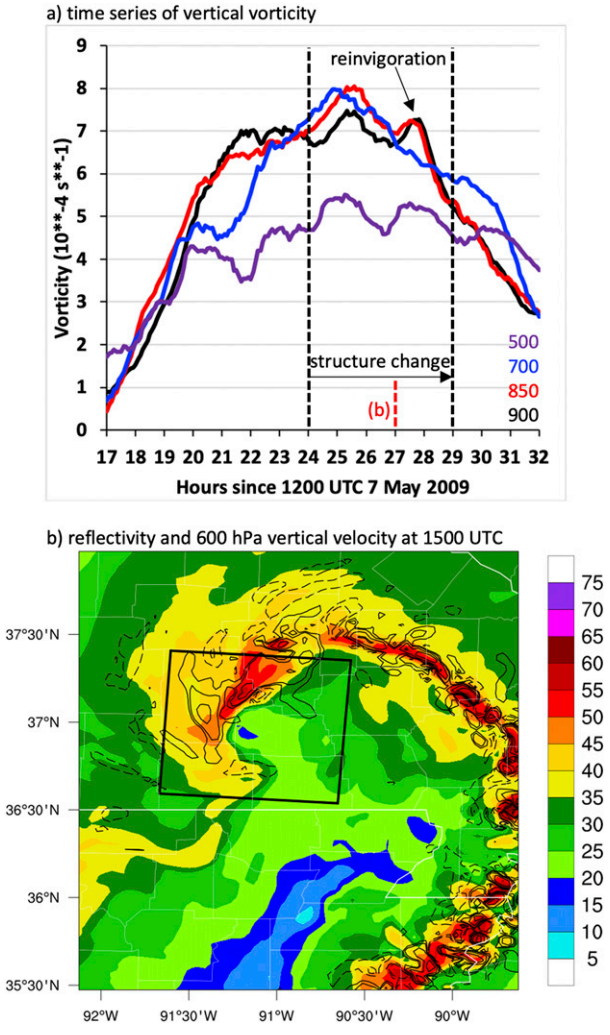

FIG. 9. The 3-km ARW (a) time series of area-mean vertical vorticity ($10^{-4}\,s^{-1}$) in a 90 km × 90 km region centered on the cyclone center at 900 (black line), 850 (red line), 700 (blue line), and 500 hPa (purple line). The period shown in Fig. 8, including a structural change (discussed in main text) and brief reinvigoration, is bounded by the dashed vertical lines. (b) Composite reflectivity (shaded according to the color bar, dBZ) and 600 hPa vertical velocity (contours at −2, −1, 1, 2, 5, 10, 20, and 40 m s^{-1}; solid >0; dashed <0) at 1500 UTC 8 May 2009 (27 h). The 90 km × 90 km region centered on the cyclone center is shown by the unfilled black box.

given time period. Also, to account for uncertainties in the exact location of the cyclone center and the overlap of convective-scale vorticity features with the edge of the vorticity budget box, a budget ensemble approach was used as described in section 2. The budget terms therefore represent ensemble averages and the degree to which the budget balances is based on the ensemble average values for each term.

The vertical profile of 240 km × 240 km area-mean total vertical vorticity change and contributions from the terms in (1) for the 3-km ARW simulation during 0300–1500 UTC is shown in Fig. 12a. The largest increases in vertical vorticity occurred below 600 hPa, approaching $3 \times 10^{-4}\,s^{-1}$ at 700 hPa. By 1500 UTC, the largest vertical vorticity values approaching $5 \times 10^{-4}\,s^{-1}$ were located in the 900–800-hPa layer with lower values aloft, resulting in a warm-core structure below 500 hPa that is consistent with the warm seclusion. Comparison of the vertical vorticity change with the accumulated tendencies from the right-hand side of (1) reveals that the balance of the budget is reasonable since the residual is generally lower than the contribution from the individual terms (Figs. 12a,b).

Increases in area-mean vertical vorticity are driven primarily area-mean convergence of absolute vorticity (i.e., stretching) below 800 hPa (Fig. 12b). This result is consistent with the vertical profile of area-integrated vertical mass flux that shows an ascent maximum at 600 hPa and convergence at low levels (Fig. 12c). The upward vertical mass flux profile is likely a combination of ascent associated with precipitation along the bent-back front near the cyclone center and possibly the adiabatic vertical motion associated with the secondary circulation on the forward flank of the upper-level trough (not shown). The eddy-flux term is also a contributor to increases in vertical vorticity below 800 hPa and the primary contributor to increases in vertical vorticity above 500 hPa (Fig. 12b). This result shows that increases in vertical vorticity in these regions is the result of the lateral transport of vertical vorticity to the cyclone center. The tilting term dominated increases in vertical vorticity in the midtroposphere and was linked to ascent along the bent-back front (Fig. 12b). The eddy-flux and tilting terms will be discussed more below.

Time-pressure plots of the vorticity budget terms in (1) shows when each term was important in driving vorticity changes during the life cycle of IOP4 (Fig. S2). The largest positive vorticity tendency occurred during the rapid intensification period 0300–1500 UTC 4 January (Figs. S2a,b). While positive contributions from stretching at low levels and tilting at midlevels were present throughout the life cycle of IOP4, the eddy-flux contribution to positive vorticity tendency was most prevalent during the rapid intensification period (Fig. S2d).

The vertical profile of the eddy-flux term, including the relative contributions along each side of the vorticity budget box, highlights how the largest positive contributions at low levels occurred along the east side of the box (Fig. 12d). Maps of 850-hPa vertical vorticity and cyclone-relative wind at 0900, 1100, and 1300 UTC shows that the positive contribution from the eddy-flux term is linked to the lateral transport of cyclonic vertical

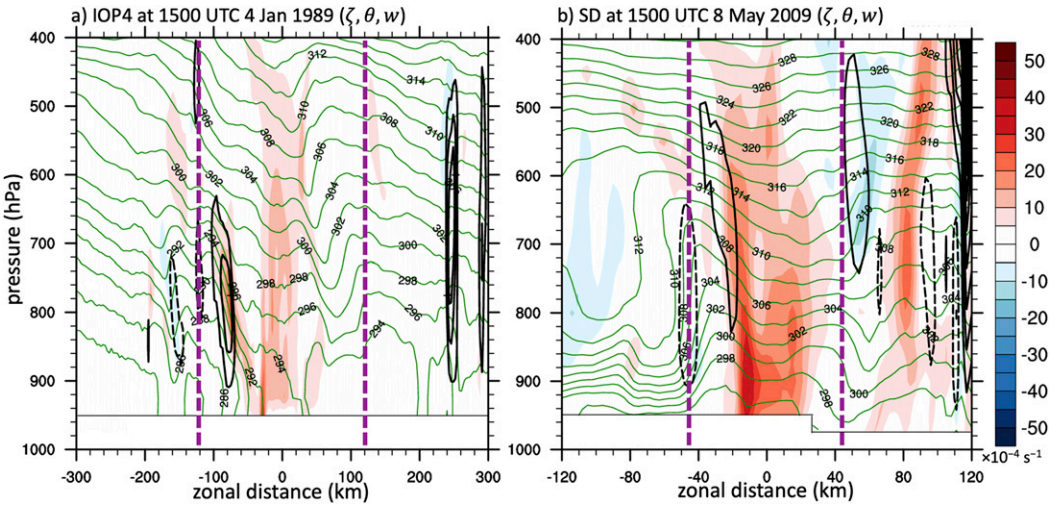

FIG. 10. Zonal vertical cross section of relative vorticity (shaded according to the color bar, $\times 10^{-4}\,s^{-1}$), potential temperature (green contours every 2 K), and vertical velocity (black contours every 0.5 m s^{-1}; ascent solid; descent dashed; zero contour omitted) for (a) IOP4 at 1500 UTC 4 Jan 1989 (15 h) and (b) the SD at 1500 UTC 8 May 2009 (27 h). The vertical dashed purple lines mark the west and east sides of the box used for the vorticity budget described in section 2. The fields plotted are averaged ±15 km in the meridional direction.

vorticity features from along the bent-back and warm fronts to the cyclone center (Figs. 13a–c). The largest contribution to positive vertical vorticity tendency at upper levels occurred on the west side of the box (Fig. 12d). The corresponding maps of 400-hPa vertical vorticity and cyclone-relative wind shows that the positive contribution is due to the lateral transport of cyclonic vorticity from the upper-level trough located west of IOP4 to the cyclone center (Figs. 13d–f). This positive contribution from the eddy-flux term at upper levels was maximized at approximately 0700–1100 UTC 4 January, then reduced in magnitude as the eastern flank of the upper-level trough moved completely over the cyclone center (Fig. S2d and Figs. 13d–f).

The lateral transport of cyclonic vertical vorticity from along the bent-back and warm fronts to the cyclone center is a result that is somewhat consistent with previous studies that showed this vorticity may be linked to the low-level wind maximum on the southwest side of the cyclone center (e.g., Schemm and Wernli 2014) or may serve as the origin of the cyclone center itself (e.g., Reed et al. 1994). The vertical vorticity budget showed that while tilting and friction contribute to negative vertical vorticity tendency at low levels during the rapid intensification of IOP4, eddy flux and system-scale stretching contribute 38% and 62%, respectively, to the total positive contributions that result in a net positive increase in vertical vorticity (Fig. 12b). This result suggests that the eddy-flux contribution is a secondary, but significant, contributor to changes in system-scale vertical vorticity at low levels for IOP4.

Inspection of individual meso-γ-scale cyclonic vertical vorticity features along the bent-back and warm fronts revealed that these features were somewhat shallow but very intense. One such vortex was identified in Figs. 14a and 14b. This vortex was trackable from 0900 to 1200 UTC 4 January 1989 and originated along the warm front almost 250 km east of the cyclone center (Fig. 13a). The vortex was advected westward by the cyclone-relative easterly flow and was trackable until it was absorbed by the main cyclone center (Figs. 13b,c). Examination of composite reflectivity at 1100 UTC 4 January shows that this vortex resembled a supercell thunderstorm (Lemon and Doswell 1979), with a hook echo-like signature in the reflectivity around the region of maximum 850-hPa relative vorticity (Figs. 14a,b). A coherent swath of hourly maximum updraft helicity[3] in the 2–5-km layer $\geq 25\,m^2\,s^{-2}$ lends additional evidence that this vortex was likely a supercell (Fig. 14a). The vertical cross section of relative vorticity, potential temperature, and vertical velocity revealed that this vortex was located in the near-surface–600-hPa layer with the highest vorticity values approaching $10^{-2}\,s^{-1}$ just above the surface (Fig. 14c).

The structure and intensity of this vortex is consistent with the small-scale vortices identified observationally by Liu et al. (1997) and Neiman et al. (1993). Liu et al. (1997,

[3] Updraft helicity in the 2–5-km layer is a common metric used in practice for determining the presence of supercells in convection-allowing simulations (Kain et al. 2008).

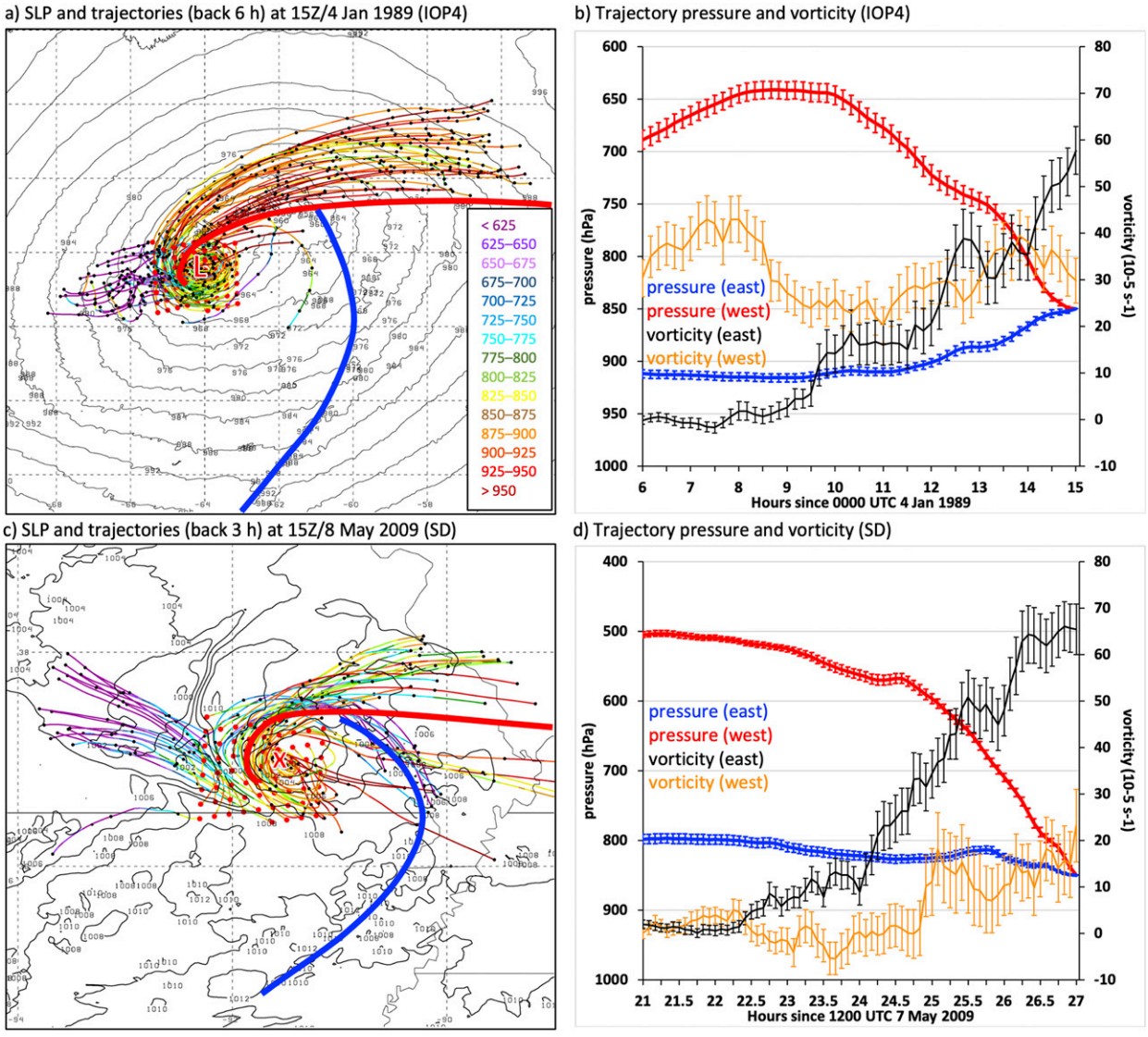

FIG. 11. (a) Sea level pressure (black contours every 4 hPa) and select (64 out of 1296) storm-relative backward air-parcel trajectories seeded at 1500 UTC 4 Jan 1989 (15 h) and (c) sea level pressure (black contours every 2 hPa) and select (64 out of 1296) storm-relative backward air-parcel trajectories seeded at 1500 UTC 8 May 2009 (27 h). The first 6 h of the 9-h backward trajectories are shown in (a). The first 3 h of the 6-h backward trajectories are shown in (c). Air-parcel trajectories are colored by air pressure (hPa) according to the key inset in (a) and hourly locations are marked by the filled black circles and the start point is marked by a red filled circle. Estimated positions of surface cold (blue) and warm (red) fronts are indicated by the curved line segments. Also shown are time series of air parcel mean pressure (hPa; left y axis) and relative vorticity (10^{-5} s^{-1}; right y axis) colored according to the key for (b) IOP4 and (d) the super derecho (SD). Error bars represent the 90% confidence interval. The subset of trajectories that originated in storm-relative space east of 60°W are classified as ''east'' (n = 631) and west of 65°W ''west'' (n = 463) for IOP4 and those that originated east of 89°W are considered ''east'' (n = 992) and west of 92°W ''west'' (n = 288) for the super derecho.

their Figs. 6 and 9) showed vortices embedded along the warm front of the IOP4 cyclone with similar intensity and vertical depth, thus verifying that these features identified in the numerical simulation were also seen in the real atmosphere. The presence of these vortices along the warm front was not surprising as the baroclinic environment was characterized by high vertical wind shear (Fig. 14d). Numerous thunderstorms resembling supercells were identified along the warm and cold fronts during the rapid intensification of IOP4 and were consistent with radar observations recorded during ERICA (Fig. 14a; Liu et al. 1997, their Fig. 3).

The positive contributions to vertical vorticity tendency by tilting of horizontal vorticity was maximized at

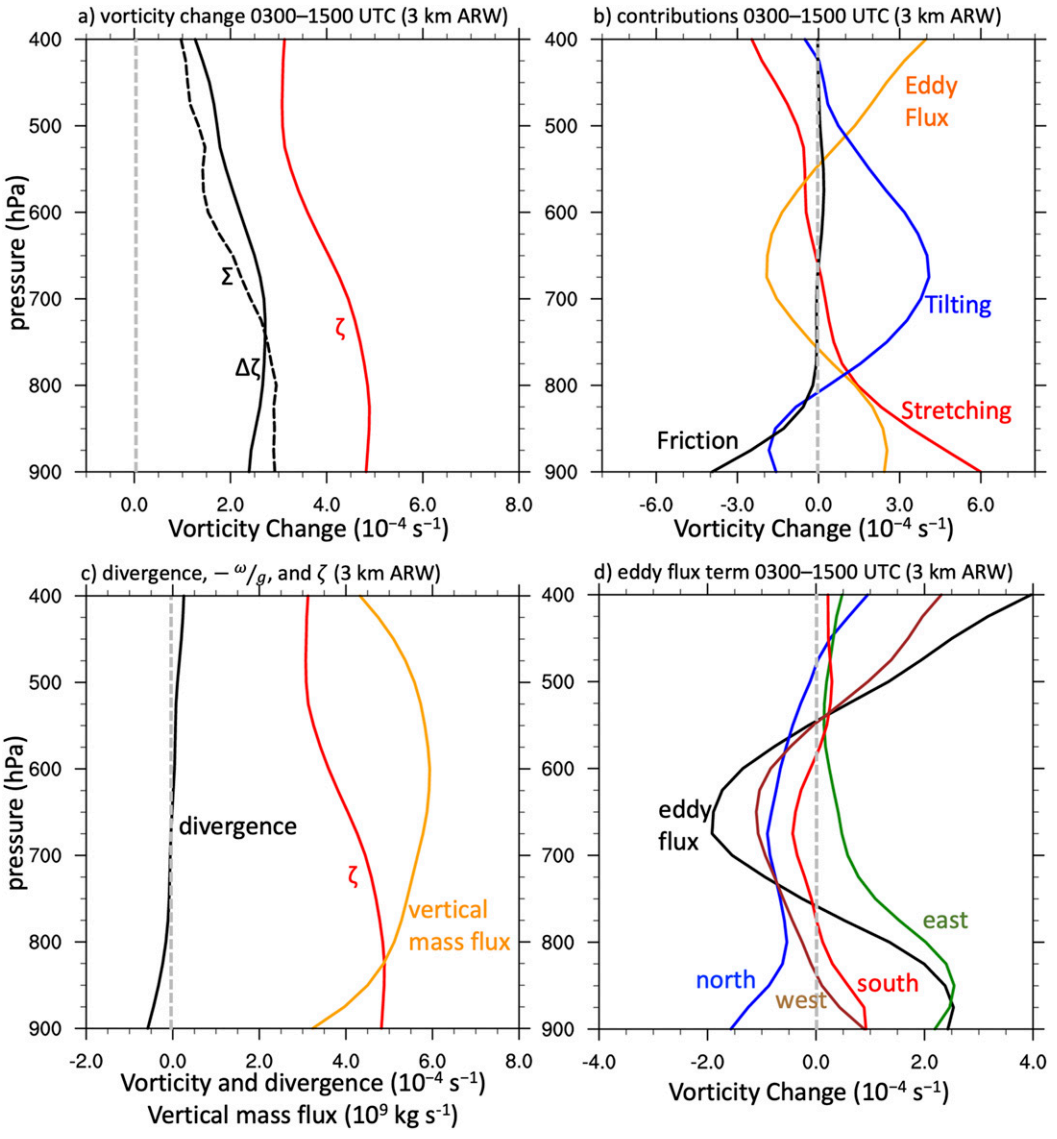

FIG. 12. Vertical profiles of 240 km × 240 km area-mean (a) final vertical vorticity (ζ; red line), vertical vorticity change ($\Delta\zeta$; black solid line), and sum of hourly rates of change of vertical vorticity from all terms on right-hand side of (1) (Σ; black dashed line); (b) sum of hourly rates of change of vertical vorticity from stretching (red line), eddy flux (orange line), tilting (blue line), and friction (black line) terms in (1); (c) final vertical vorticity (ζ; red line), time-mean divergence (black line), and time-mean area-integrated vertical mass flux (10^9 kg s^{-1}; orange line); and (d) total (black) and contributions to vorticity change along each side of the 240 km × 240 km region (north in blue; east in green; south in red; west in brown) for the eddy-flux term for IOP4 in the 3-km ARW simulation at 0300–1500 UTC 4 Jan 1989 (3–15 h). The units for all variables except vertical mass flux are 10^{-4} s^{-1}.

midlevels near 675 hPa (Fig. 12b). The positive contributions occurred primarily where the bent-back front intersected the north side of the vertical vorticity budget box (Fig. S3 and Fig. 15a). In this region, horizontal vortex lines pointed north and northwestward out of the vorticity budget box where a region of ascent was located at the edge of the box, resulting in a positive vertical vorticity tendency in the box (Fig. 15a). The north and northwestward orientation of the horizontal vortex lines was associated with the southwesterly vertical wind shear in conjunction with stronger southwesterly flow aloft ahead of the upper-level trough (Figs. 13f and 15a). At low levels, tilting of horizontal vorticity along the north side of the budget box was not a contributor to positive vertical vorticity tendency on the system scale (Fig. S3). The stream of vortex lines aligned with the bent-back and warm fronts were likely tilted by ascent closer to the cyclone center (Fig. 15b). Because

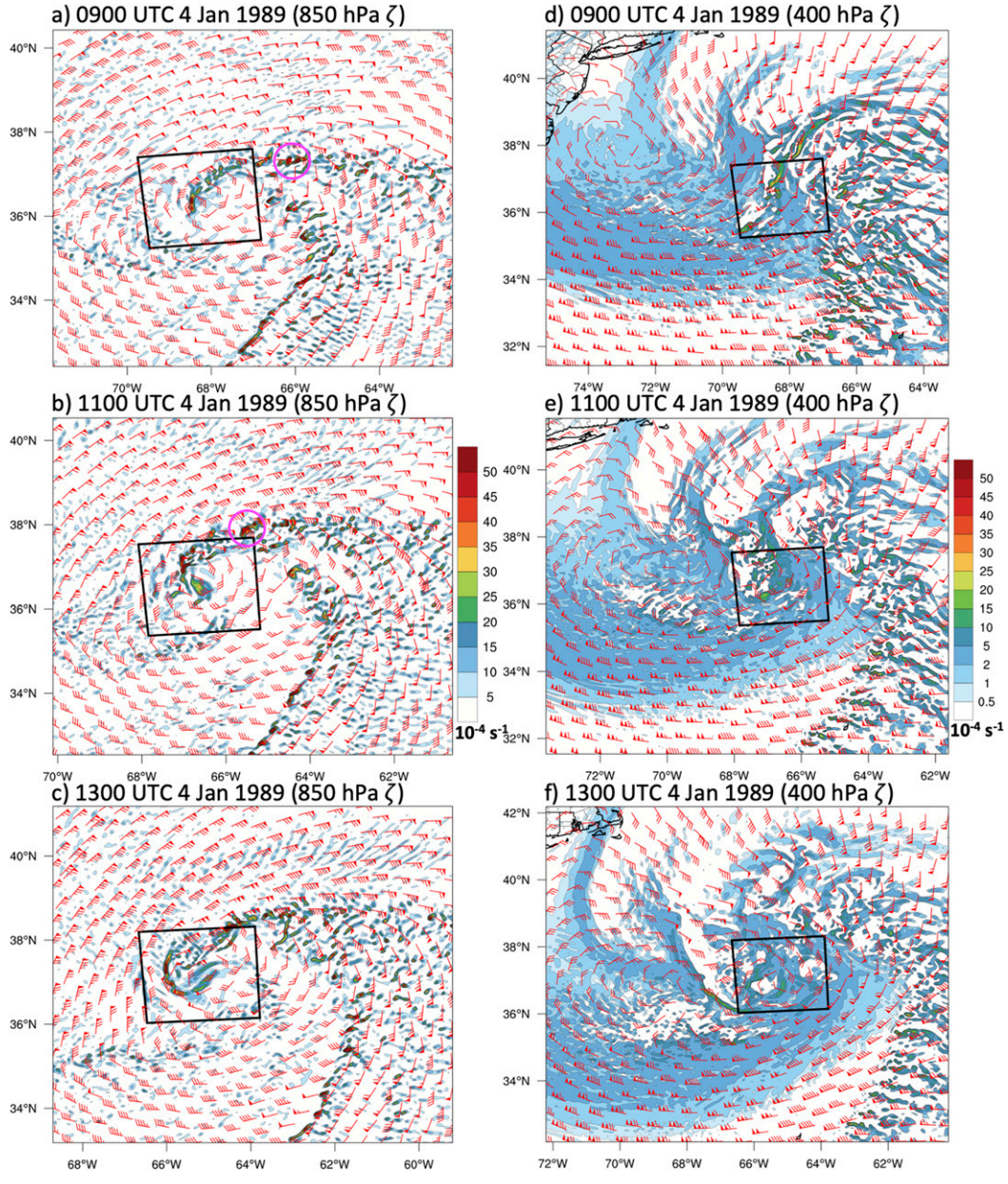

FIG. 13. The 850-hPa vertical vorticity (shaded according to the color bar, 10^{-4} s^{-1}) and cyclone-relative wind (barbs as in Fig. 5) from the 3-km ARW simulation of IOP4 at (a) 0900 (9 h), (b) 1100 (11 h), and (c) 1300 UTC 4 Jan 1989 (13 h). (d)–(f) As in (a)–(c), but at 400 hPa. The 240 km × 240 km region centered on the cyclone center is shown by the unfilled black box. The intense cyclonic vorticity feature shown in Fig. 14 is marked by the unfilled magenta circle in (a) and (b).

the tilting of this horizontal vorticity was entirely within the box, it resulted in a net zero vertical vorticity tendency on the scale of the budget box. Tilting at may be important, however, for the generation of low-level vertical vorticity at smaller scales near the center of the cyclone based on the configuration where the horizontal vortex lines are aligned with the cyclone-relative wind along the bent-back and warm fronts (Fig. 15b). This configuration is a larger-scale analogy to the streamwise vorticity current that occurs along the forward flank downdraft gust front in supercell thunderstorms, documented to be important in the generation of low-level mesocyclones (e.g., Rotunno and Klemp 1985).

b. *Super derecho*

Given the brief reintensification of the low-level vertical vorticity of the super derecho as it acquired characteristics of a warm seclusion cyclone, a vertical

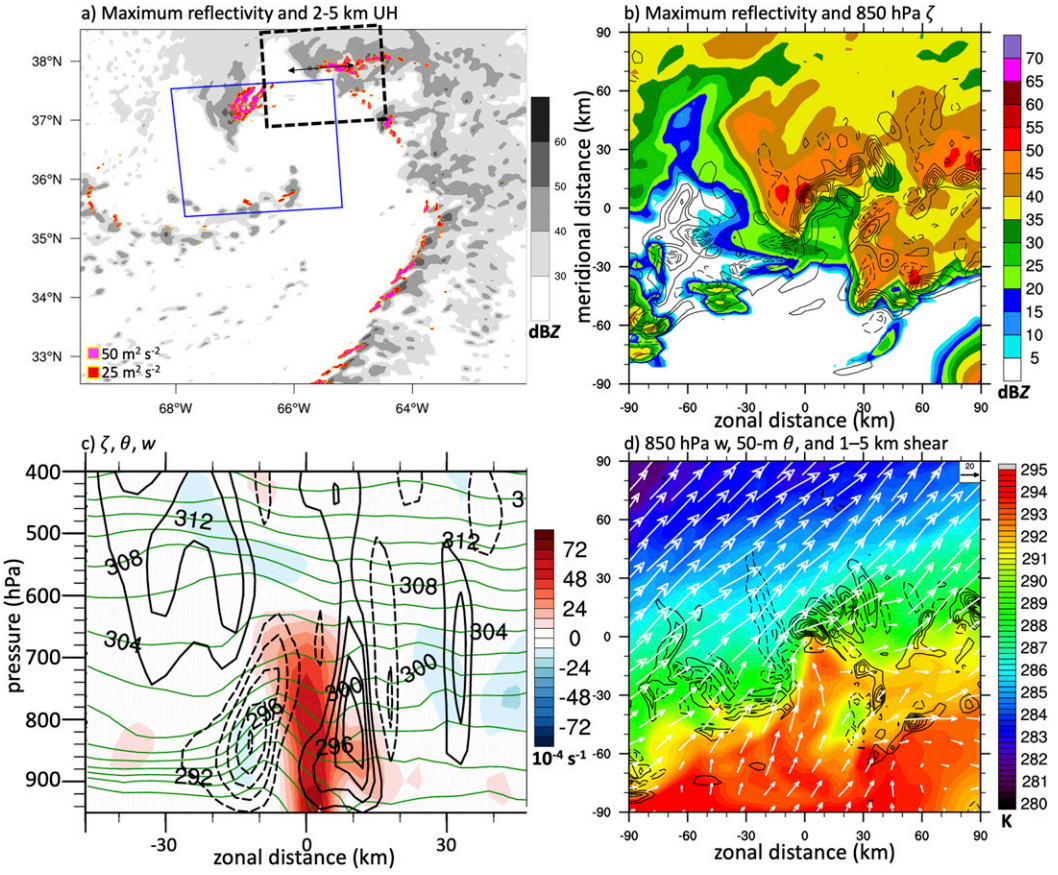

FIG. 14. The 3-km ARW simulated (a) composite reflectivity (shaded according to the grayscale, dBZ) and hourly-maximum updraft helicity in the 2–5-km layer (shaded according to the key in the lower-left corner, $m^2 s^{-2}$); (b) composite reflectivity (shaded according to the color bar, dBZ) and 850-hPa vertical vorticity (contours every $10 \times 10^{-4} s^{-1}$; zero contour omitted; positive solid; negative dashed); (c) zonal vertical cross section of relative vorticity (shaded according to the color bar, $10^{-4} s^{-1}$), potential temperature (green contours every 2 K), and vertical velocity (black contours every 0.5 m s^{-1}; zero contour omitted; descent dashed; ascent solid); and (d) 850-hPa vertical velocity (contours every 1 m s^{-1}; zero contour omitted; ascent solid; descent dashed), 50-m potential temperature (shaded according to the color bar, K), and bulk vertical wind shear in the 1–5-km layer (arrows in m s^{-1}) for IOP4 at 1100 UTC 4 Jan 1989 (11 h). Orientation of the cross section in (c) is shown by the double-sided black arrow in (a). The 240 km × 240 km region centered on the cyclone center is shown by the unfilled blue box in (a). The unfilled black dashed box in (a) marks the region shown in (b) and (d).

vorticity budget is used to determine the vorticity dynamics contributing to this intensification. Evans et al. (2014) also computed a vertical vorticity budget using (1) for the super derecho. Despite the minor differences in methodology, comparison of the time-pressure plots of the budget terms reveals similar results (compare Fig. S4 with Figs. 11 and 12 in Evans et al.). The primary focus of the Evans et al. study was the development and intensification of the bookend vortex through its peak intensity near 1330 UTC 8 May 2009. While the current study has overlap with Evans et al. we focus on the brief reinvigoration of the super derecho vortex later in its life cycle at 1500–1600 UTC when it acquired structural characteristics of a warm seclusion.

The reinvigoration of the super derecho bookend vortex began at 1500 UTC and reached a peak vertical vorticity at 900 hPa at 1535 UTC 8 May (Fig. 9a). The vertical vorticity budget is computed using the 5-min output for 1500–1535 UTC. The instantaneous tendencies for each term are multiplied by 300 s to convert the units from s^{-2} to s^{-1} $(5\,\text{min})^{-1}$, then are added over the budget period to get the total contribution to vorticity change. The vertical profile of the budget terms in (1) shows good agreement with the actual vorticity change during the period, with vorticity increasing beneath 800 hPa and above 650 hPa and decreasing in the 800–650-hPa layer (Fig. 16a). Tilting of horizontal vorticity is the primary contributor to positive vertical vorticity

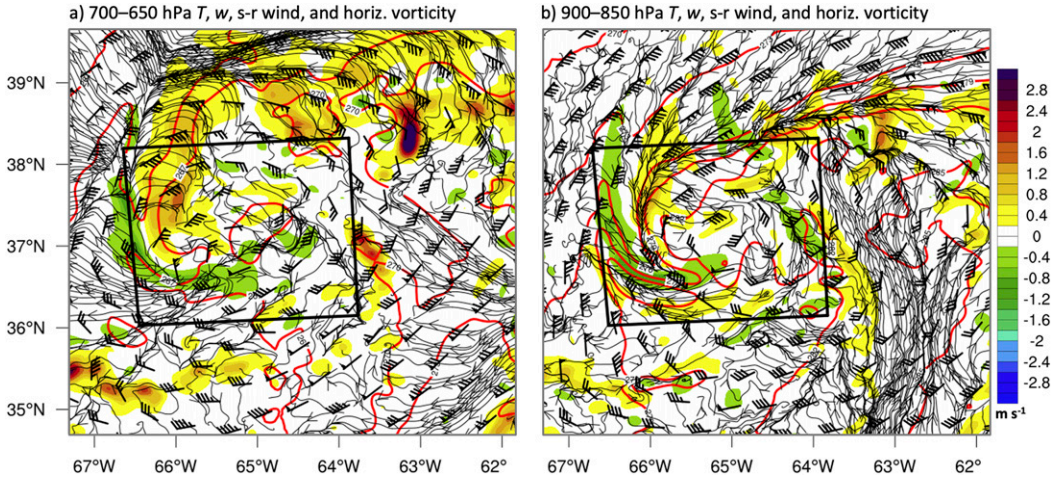

FIG. 15. Temperature (red contours every 3 K), cyclone-relative wind (barbs as in Fig. 5), vertical velocity (shaded according to the color bar, m s^{-1}), and horizontal vorticity streamlines (thin black streamlines with arrows) in the (a) 700–650- and (b) 900–850-hPa layer from the 3-km ARW simulation of IOP4 at 1300 UTC 4 Jan 1989 (13 h). The 240 km × 240 km region centered on the cyclone center is shown by the unfilled black box.

changes above 550 hPa, where ascent along the northern edge of the vorticity budget box tilts horizontal vorticity associated with westerly vertical wind shear (Fig. 9b and Fig. S5). Tilting contributes to a negative vorticity tendency below 700 hPa on the scale of the vorticity budget box; however, somewhat similar to IOP4 there is a region of streamwise vorticity on the north and east side of the cyclone center that may contribute to increases in 900–850-hPa vertical vorticity near the center (Fig. 17). Streamwise vorticity at 900 hPa was also present at earlier times prior to the warm seclusion stage of the super derecho (Weisman et al. 2013, their Figs. 20a,c). Area-mean stretching is the primary contributor to positive vorticity tendency in the 850–550-hPa layer and is associated with a relatively deep layer of convergence beneath the maximum box-integrated upward vertical mass flux at 550 hPa (Figs. 16b,c). The upward vertical mass flux was a signature of intense convection near the center of the super derecho (Fig. 9b).

The contributions to positive vorticity changes below 850 hPa were driven primarily by the eddy-flux term (Fig. 16b). Cyclonic vertical vorticity was laterally transported from along the leading convective line to the super derecho cyclone center by the easterly cyclone-relative winds (Figs. 18a,b). The transport of the positive vertical vorticity into the east side of the budget box and the transport of negative vertical vorticity out of the west and south sides of the budget box contributed to the large positive contribution from the eddy-flux term at low levels (Fig. 16d). At midlevels, the large positive contribution to vertical vorticity tendency from the stretching and tilting terms was offset by a large negative contribution by the eddy-flux term (Fig. 16b). The negative contribution from the eddy-flux term was associated primarily with the inward flux of negative vorticity at 650 hPa along the western half of the north side of the box and on the eastern half of the south side of the box between 1500 and 1535 UTC (Figs. 18c,d).

c. *Comparison of vorticity budget results*

The vorticity budget analysis highlighted key similarities and differences in the processes that contributed to increases in system-scale vertical vorticity for IOP4 and the super derecho. The notable differences in processes driving changes in system-scale vertical vorticity occurred primarily above 800 hPa. The lateral transport of vertical vorticity from the upper-level trough to the cyclone center was the primary contributor to increases in system-scale vertical vorticity above 500 hPa for IOP4 (Fig. 12b). Tilting of horizontal vorticity along the bent-back front was the primary contributor to increases in vertical vorticity for the super derecho above 500 hPa (Fig. 16b). The unimportance of the eddy-flux term above 500 hPa for the super derecho is likely in response to the presence of a weaker upper-level disturbance to the west compared to IOP4 (Figs. 5 and 7). Differences in the key processes driving changes in system-scale vertical vorticity were also apparent in the 800–500-hPa layer. Tilting of horizontal vorticity along the bent-back front was important for IOP4, while system-scale stretching associated with intense convection near the cyclone center was key for the super derecho. Additionally, the positive contributions to vorticity tendency from stretching was balanced by a large negative contribution from the eddy-flux term associated with the

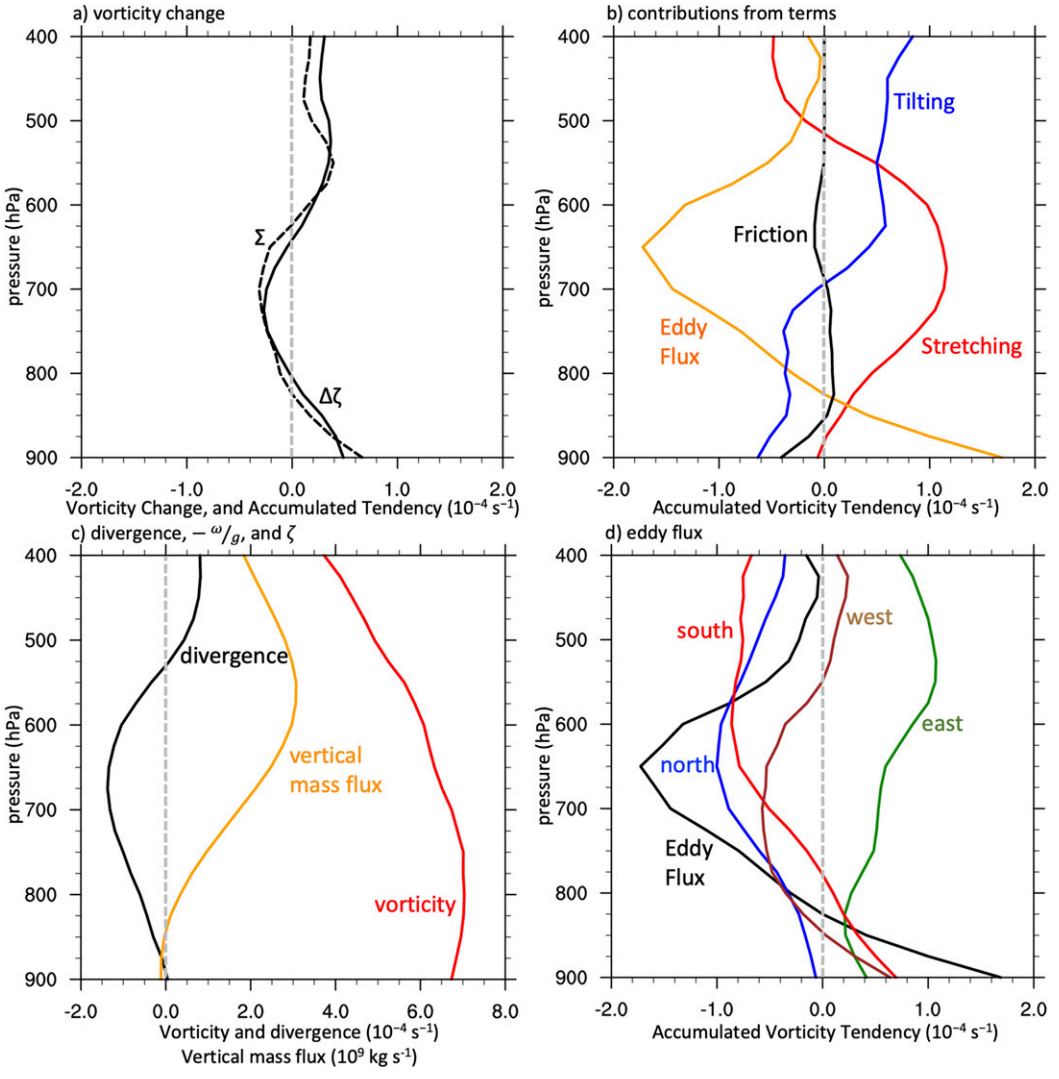

FIG. 16. Vertical profiles of 90 km × 90 km area-mean (a) vertical vorticity change ($\Delta\zeta$; black solid line) and sum of hourly rates of change of vertical vorticity from all terms on right-hand side of (1) (Σ; black dashed line); (b) sum of hourly rates of change of vertical vorticity from stretching (red line), eddy flux (orange line), tilting (blue line), and friction (black line) terms in (1); (c) final vertical vorticity (ζ; red line), time-mean divergence (black line), and time-mean area-integrated vertical mass flux (10^9 kg s^{-1}; orange line); and (d) total (black) and contributions to vorticity change along each side of the 90 km × 90 km region (north in blue; east in green; south in red; west in brown) for the eddy-flux term in (1) for the super derecho at 1500–1535 UTC 8 May 2009 (27–27.58 h). The units for all variables except vertical mass flux are 10^{-4} s^{-1}.

lateral transport of negative vorticity to the super derecho center.

The key similarities between IOP4 and the super derecho are at low levels beneath 800 hPa. For both systems, system-scale stretching and eddy flux are the contributors to increases while tilting and friction are contributors to decreases in system-scale vertical vorticity (Figs. 12b and 16b). The accumulated vorticity tendencies in the 900–800-hPa layer for stretching and eddy flux during the rapid intensification period of IOP4 were 3.6×10^{-4} s^{-1} and 2.1×10^{-4} s^{-1}, respectively. The combined accumulated tendency of these terms was 5.7×10^{-4} s^{-1} (62% from stretching and 38% from eddy flux), which offset the accumulated tendency from tilting and friction of -2.8×10^{-4} s^{-1}, resulting in a net positive vorticity change of 2.9×10^{-4} s^{-1}. For the intensification of the super derecho, stretching and eddy flux contributed to a vorticity change of 0.2×10^{-4} and 0.6×10^{-4} s^{-1} resulting in a combined accumulated vorticity tendency of 0.8×10^{-4} s^{-1} (23% from stretching and 77% from eddy flux). The positive contributions from stretching and eddy flux compensated for an

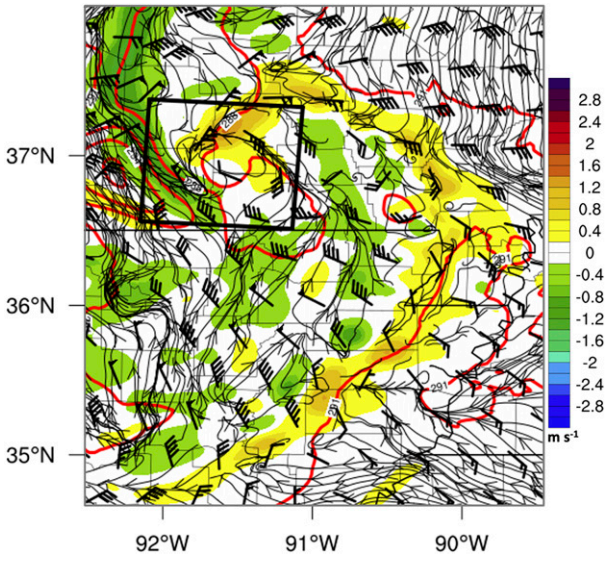

FIG. 17. Temperature (red contours every 3 K), cyclone-relative wind (barbs as in Fig. 5), vertical velocity (shaded according to the color bar, m s^{-1}), and horizontal vorticity streamlines (thin black streamlines with arrows) in the 900–850-hPa layer from the 3-km ARW simulation of the super derecho at 1500 UTC 8 May 2009 (27 h). The 90 km × 90 km region centered on the cyclone center is shown by the unfilled black box.

accumulated tendency from tilting and friction of $-0.5 \times 10^{-4}\,s^{-1}$, resulting in a net positive vorticity change of $0.3 \times 10^{-4}\,s^{-1}$.

In all, the vorticity budget analysis shows that IOP4 and the super derecho were most similar at low levels, which is consistent with the noted structural similarities of the fronts and low-level warm seclusion. For both cases, increases in system-scale vertical vorticity of the low-level warm seclusion center were driven by system-scale stretching and eddy flux. The latter contribution represents the lateral transport of positive vertical vorticity from along the bent-back and warm fronts to the cyclone center. This process was a secondary, but significant, contributor to intensification of IOP4 and was the primary contributor to intensification of the super derecho.

5. Concluding discussion

This study used convection-allowing ARW simulations and a vorticity budget to examine the vorticity dynamics driving the intensification of the oceanic bomb cyclone of 4–5 January 1989 and the super derecho of 8 May 2009. The former was a synoptic-scale warm seclusion extratropical cyclone (Shapiro and Keyser 1990) that occurred in the western North Atlantic and was sampled by IOP4 of the ERICA field program. The latter was a warm-season derecho that occurred in the southern plains and Mississippi valley (Weisman et al. 2013). While these weather systems are of different scale and origin, they both developed an intense surface cyclone with similar overall airstreams and frontal structure, warm air secluded from the warm sector, and an intense low-level jet on the southwest side of the surface low pressure center. The development of a warm seclusion in these two cases prompted questions on whether the processes that led to increases in system-scale vorticity during the warm seclusion process were similar, despite the inherent differences in scale between these two cyclones. Both systems intensified while the warm seclusion center was cut off from the warm sector, an evolution similar to that shown in analysis of the infamous 1992 New Year's Day Storm warm seclusion cyclone in Norway by Spensberger and Schemm (2020).

The key processes that drive increases in system-scale vertical vorticity for the IOP4 cyclone are eddy flux at upper levels, tilting at midlevels, and eddy flux and system-scale stretching at low levels. The eddy-flux contribution to increases in vertical vorticity aloft is associated with the approach of the upper-level trough to the west during cyclonic wave breaking (Thorncroft et al. 1993). The tilting of horizontal vorticity along the bent-back frontal zone is important in driving increases in system-scale vorticity at midlevels. At low levels beneath 800 hPa, stretching driven by mean convergence contributed to 62% of the positive contribution to increases in system-scale vorticity. The eddy-flux term contributed the remaining 38% of the positive contribution to increases in system-scale vertical vorticity and was associated with the lateral transport of cyclonic vertical vorticity from along the bent-back and warm fronts to the cyclone center. A subset of the cyclonic vertical vorticity features along these fronts were particularly intense, consistent with observations during ERICA (Neiman et al. 1993; Wakimoto et al. 1995; Liu et al. 1997), and resembled supercells.

The lateral transport of vertical vorticity to near the cyclone center has been documented in previous studies (e.g., Takayabu 1986). Reed et al. (1994) suggested that the vorticity along the bent-back front can fracture and evolve into the cyclone center. The eddy-flux contribution shown by the vorticity budget is linked to the cyclone-relative easterly flow at low levels that drives the lateral transport of cyclonic vorticity along the bent-back and warm front to the cyclone center. This easterly flow is associated with the cold conveyor belt (Carlson 1980) and has been linked in earlier studies to the lateral transport of positive PV from along the warm front to near the intense low-level jet commonly seen on the southwest flank of the cyclone center (Schemm and Wernli 2014). The vorticity budget presented here shows

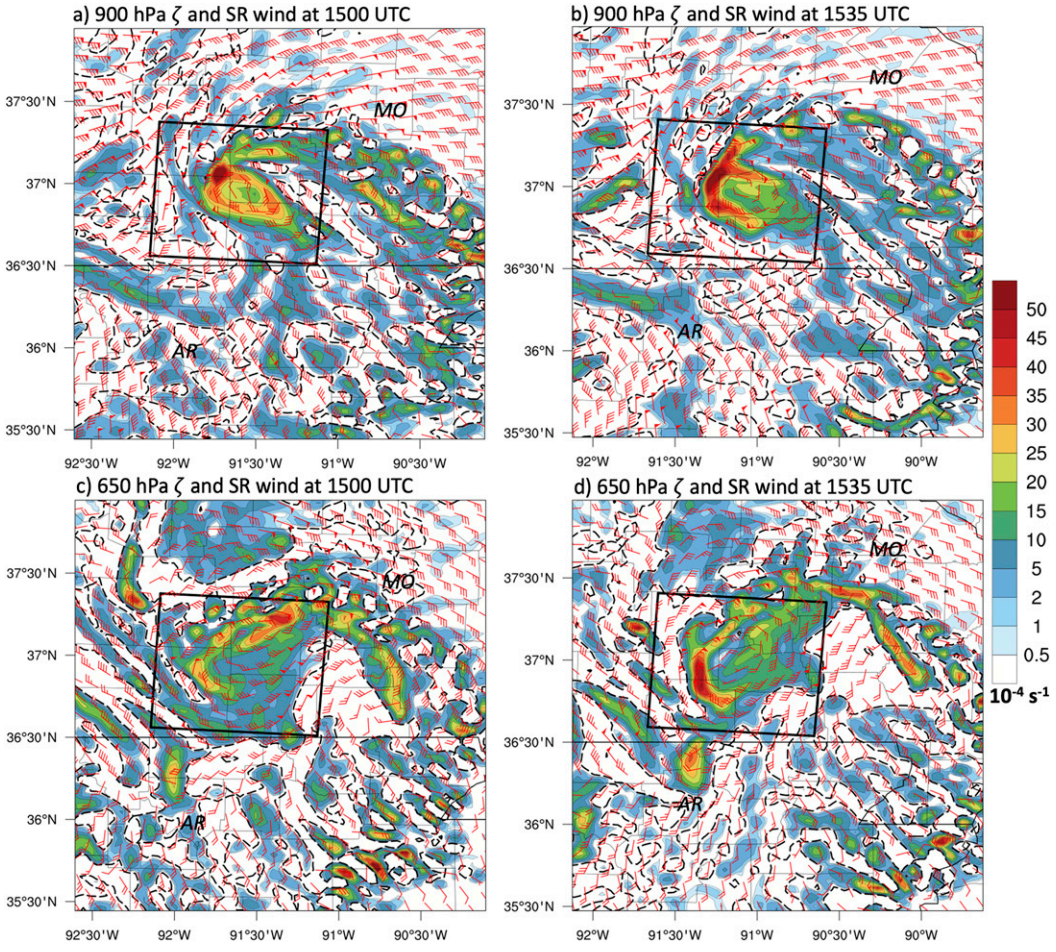

FIG. 18. The 900 hPa vertical vorticity (shaded according to the color bar, $10^{-4}\,s^{-1}$; dashed contour at $-2 \times 10^{-5}\,s^{-1}$) and cyclone-relative wind (barbs as in Fig. 5) from the 3-km ARW simulation of the super derecho at (a) 1500 (27 h) and (b) 1535 UTC 8 May 2009 (27.58 h). (c),(d) As in (a) and (b), but at 650 hPa. The 90 km × 90 km region centered on the cyclone center is shown by the unfilled black box.

that this process, while secondary to system-scale stretching, is significant for the intensification of the IOP4 cyclone.

A brief reinvigoration of the super derecho occurred as it developed characteristics of a warm seclusion cyclone. The vorticity budget analysis during the reinvigoration revealed that increases in system-scale vertical vorticity were linked to tilting and system-scale stretching at upper and midlevels. This result differs from the IOP4 cyclone, which was driven by eddy flux and tilting and upper and midlevels, and may be associated with the lack of a strong upper-level trough west of the super derecho. At low levels, however, the eddy-flux term was the primary contributor to positive vertical vorticity changes during the reinvigoration of the super derecho. Cyclonic vertical vorticity features along the cold pool gust front and warm front were laterally transported toward the cyclone center by easterly system-relative flow, thereby representing the positive contribution to vorticity tendency by the eddy-flux term. This result is similar to the vorticity budget for the IOP4 cyclone.

The common process that contributes to increases in system-scale cyclonic vertical vorticity for the IOP4 and super derecho cyclones is the lateral transport of cyclonic vorticity westward to the cyclone center. This vorticity originates along the bent-back and warm fronts for IOP4 and the warm front and cold pool gust-front boundary for the super derecho. A similar lateral transport of vertical vorticity was documented during the extratropical transition of intensifying Hurricane Sandy in 2012 (Galarneau et al. 2013). The lateral transport of low-level vertical vorticity has also been shown to be a key component in developing an intense mesoscale convective vortex in which the cyclonic circulation reaches the ground beneath the midlevel circulation

(Davis and Galarneau 2009). In all, we hypothesize that among a wide array of intense cyclonic systems ranging from warm seclusion extratropical cyclones to some mesoscale convective systems, there is a common thread that emerges with regard to the processes that drive increases in system-scale cyclonic vertical vorticity. Vertical vorticity that originates along surface boundaries away from the cyclone center is laterally transported by the cyclone-relative wind and accumulated at the cyclone center, thereby contributing to overall increases in system-scale vertical vorticity during intensification.

Acknowledgments. The authors thank Mel Shapiro for his insights on IOP4 and for being an inspiration in studying the life cycle of extratropical cyclones. We thank three anonymous reviewers for their valuable criticisms that contributed to updates from the initial version of the paper. This study benefitted from conversations with Dan Keyser. Mike Coniglio provided comments on an earlier version of the manuscript. ARW simulations were generated using NCAR's supercomputing resource. Support was provided by NOAA/OAR under NOAA–University of Oklahoma Cooperative Agreement NA16OAR4320115, U.S. Department of Commerce. The National Center for Atmospheric Research is sponsored by the National Science Foundation.

Data availability statement. The European Centre for Medium-Range Weather Forecasts (ECMWF) interim reanalysis (ERA-Interim; https://www.ecmwf.int) was used for the initial and lateral boundary condition for the simulations of IOP4. Availability of the ERA-Interim are subject to the policies of ECMWF. All other datasets used in this study are publicly available at the National Centers for Environmental Information (https://www.ncdc.noaa.gov/). All simulations were generated using the publicly available ARW model (http://wrf-model.org). All calculations were performed using NCAR Command Language (https://www.ncl.ucar.edu/) and General Meteorology Package (https://www.unidata.ucar.edu/software/gempak/). The air parcel trajectories were computed using Read/Interpolate/Plot (https://www2.mmm.ucar.edu/wrf/users/docs/ripug.htm). These software packages are publicly available.

REFERENCES

Atkins, N. T., and M. St. Laurent, 2009: Bow echo mesovortices. Part I: Processes that influence their damaging potential. *Mon. Wea. Rev.*, **137**, 1497–1513, https://doi.org/10.1175/2008MWR2649.1.

Bjerknes, J., 1919: On the structure of moving cyclones. *Mon. Wea. Rev.*, **47**, 95–99, https://doi.org/10.1175/1520-0493(1919)47<95:OTSOMC>2.0.CO;2.

——, and H. Solberg, 1922: Life cycle of cyclones and the polar front theory of atmospheric circulation. *Geofys. Publ.*, **3**, 3–18, http://www.ngfweb.no/docs/NGF_GP_Vol03_no1.pdf.

Blier, W., and R. M. Wakimoto, 1995: Observations of the early evolution of an explosive oceanic cyclone during ERICA IOP 5. Part I: Synoptic overview and mesoscale frontal structure. *Mon. Wea. Rev.*, **123**, 1288–1310, https://doi.org/10.1175/1520-0493(1995)123<1288:OOTEEO>2.0.CO;2.

Browning, K. A., 2004: The sting at the end of the tail: Damaging winds associated with extratropical cyclones. *Quart. J. Roy. Meteor. Soc.*, **130**, 375–399, https://doi.org/10.1256/qj.02.143.

Carlson, T. N., 1980: Airflow through midlatitude cyclones and the comma cloud pattern. *Mon. Wea. Rev.*, **108**, 1498–1509, https://doi.org/10.1175/1520-0493(1980)108<1498:ATMCAT>2.0.CO;2.

Clark, A. J., W. A. Gallus, M. Xue, and F. Kong, 2010: Convection-allowing and convection-parameterizing ensemble forecasts of a mesoscale convective vortex and associated severe weather environment. *Wea. Forecasting*, **25**, 1052–1081, https://doi.org/10.1175/2010WAF2222390.1.

Coniglio, M. C., and D. J. Stensrud, 2004: Interpreting the climatology of derechos. *Wea. Forecasting*, **19**, 595–605, https://doi.org/10.1175/1520-0434(2004)019<0595:ITCOD>2.0.CO;2.

——, S. F. Corfidi, and J. S. Kain, 2011: Environment and early evolution of the 8 May 2009 derecho-producing convective system. *Mon. Wea. Rev.*, **139**, 1083–1102, https://doi.org/10.1175/2010MWR3413.1.

——, ——, and ——, 2012: Views on applying RKW theory: An illustration using the 8 May 2009 derecho-producing convective system. *Mon. Wea. Rev.*, **140**, 1023–1043, https://doi.org/10.1175/MWR-D-11-00026.1.

Corfidi, S. F., M. C. Coniglio, A. E. Cohen, and C. M. Mead, 2016: A proposed revision to the definition of "derecho." *Bull. Amer. Meteor. Soc.*, **97**, 935–949, https://doi.org/10.1175/BAMS-D-14-00254.1.

Davis, C. A., and M. L. Weisman, 1994: Balanced dynamics of mesoscale vortices produced in simulated convective systems. *J. Atmos. Sci.*, **51**, 2005–2030, https://doi.org/10.1175/1520-0469(1994)051<2005:BDOMVP>2.0.CO;2.

——, and L. F. Bosart, 2003: Baroclinically induced tropical cyclogenesis. *Mon. Wea. Rev.*, **131**, 2730–2747, https://doi.org/10.1175/1520-0493(2003)131<2730:BITC>2.0.CO;2.

——, and T. J. Galarneau, 2009: The vertical structure of mesoscale convective vortices. *J. Atmos. Sci.*, **66**, 686–704, https://doi.org/10.1175/2008JAS2819.1.

——, and Coauthors, 2008: Prediction of landfalling hurricanes with the Advanced Hurricane WRF Model. *Mon. Wea. Rev.*, **136**, 1990–2005, https://doi.org/10.1175/2007MWR2085.1.

Evans, C., M. L. Weisman, and L. F. Bosart, 2014: Development of an intense, warm-core mesoscale vortex associated with the 8 May 2009 "super derecho" convective event. *J. Atmos. Sci.*, **71**, 1218–1240, https://doi.org/10.1175/JAS-D-13-0167.1.

Evans, J. S., and C. A. Doswell, 2001: Examination of derecho environments using proximity soundings. *Wea. Forecasting*, **16**, 329–342, https://doi.org/10.1175/1520-0434(2001)016<0329:EODEUP>2.0.CO;2.

Fortune, M. A., W. R. Cotton, and R. L. McAnelly, 1992: Frontal-wave-like evolution in some mesoscale convective complexes. *Mon. Wea. Rev.*, **120**, 1279–1300, https://doi.org/10.1175/1520-0493(1992)120<1279:FWLEIS>2.0.CO;2.

Fujita, T., 1955: Results of detailed synoptic studies of squall lines. *Tellus*, **7**, 405–436, https://doi.org/10.3402/tellusa.v7i4.8920.

Galarneau, T. J., Jr., L. F. Bosart, C. A. Davis, and R. McTaggart-Cowan, 2009: Baroclinic transition of a long-lived mesoscale

convective vortex. *Mon. Wea. Rev.*, **137**, 562–584, https://doi.org/10.1175/2008MWR2651.1.

——, C. A. Davis, and M. A. Shapiro, 2013: Intensification of Hurricane Sandy (2012) through extratropical warm core seclusion. *Mon. Wea. Rev.*, **141**, 4296–4321, https://doi.org/10.1175/MWR-D-13-00181.1.

Grønås, S., 1995: The seclusion intensification of the New Year's Day storm 1992. *Tellus*, **47A**, 733–746, https://doi.org/10.3402/tellusa.v47i5.11571.

Grunzke, C. T., and C. Evans, 2017: Predictability and dynamics of warm-core mesoscale vortex formation with the 8 May 2009 "super derecho" event. *Mon. Wea. Rev.*, **145**, 811–832, https://doi.org/10.1175/MWR-D-16-0217.1.

Guastini, C. T., and L. F. Bosart, 2016: Analysis of a progressive derecho climatology and associated formation environments. *Mon. Wea. Rev.*, **144**, 1363–1382, https://doi.org/10.1175/MWR-D-15-0256.1.

Hadlock, R., and C. W. Kreitzberg, 1988: The Experiment on Rapidly Intensifying Cyclones over the Atlantic (ERICA) field study: Objectives and plans. *Bull. Amer. Meteor. Soc.*, **69**, 1309–1320, https://doi.org/10.1175/1520-0477(1988)069<1309:TEORIC>2.0.CO;2.

Harr, P. A., and R. L. Elsberry, 2000: Extratropical transition of tropical cyclones over the western North Pacific. Part I: Evolution of structural characteristics during the transition process. *Mon. Wea. Rev.*, **128**, 2613–2633, https://doi.org/10.1175/1520-0493(2000)128<2613:ETOTCO>2.0.CO;2.

Johns, R. H., and W. D. Hirt, 1987: Derechos: Widespread convectively induced windstorms. *Wea. Forecasting*, **2**, 32–49, https://doi.org/10.1175/1520-0434(1987)002<0032:DWCIW>2.0.CO;2.

Kain, J. S., and Coauthors, 2008: Some practical considerations regarding horizontal resolution in the first generation of operational convection-allowing NWP. *Wea. Forecasting*, **23**, 931–952, https://doi.org/10.1175/WAF2007106.1.

Knapp, K. R., and Coauthors, 2011: Globally Gridded Satellite (GridSat) observations for climate studies. *Bull. Amer. Meteor. Soc.*, **92**, 893–907, https://doi.org/10.1175/2011BAMS3039.1.

Lemon, L. R., and C. A. Doswell, 1979: Severe thunderstorm evolution and mesocyclone structure as related to tornadogenesis. *Mon. Wea. Rev.*, **107**, 1184–1197, https://doi.org/10.1175/1520-0493(1979)107<1184:STEAMS>2.0.CO;2.

Liu, C.-H., R. M. Wakimoto, and F. Roux, 1997: Observations of mesoscale circulations within extratropical cyclones over the North Atlantic Ocean during ERICA. *Mon. Wea. Rev.*, **125**, 341–364, https://doi.org/10.1175/1520-0493(1997)125<0341:OOMCWE>2.0.CO;2.

Mazza, E., U. Ulbrich, and R. Klein, 2017: The tropical transition of the October 1996 Medicane in the western Mediterranean sea: A warm seclusion event. *Mon. Wea. Rev.*, **145**, 2575–2595, https://doi.org/10.1175/MWR-D-16-0474.1.

Neiman, P. J., and M. A. Shapiro, 1993: The life cycle of an extratropical marine cyclone. Part I: Frontal-cyclone evolution and thermodynamic air–sea interaction. *Mon. Wea. Rev.*, **121**, 2153–2176, https://doi.org/10.1175/1520-0493(1993)121<2153:TLCOAE>2.0.CO;2.

——, ——, and L. S. Fedor, 1993: The life cycle of an extratropical marine cyclone. Part II: Mesoscale structure and diagnostics. *Mon. Wea. Rev.*, **121**, 2177–2199, https://doi.org/10.1175/1520-0493(1993)121<2177:TLCOAE>2.0.CO;2.

Reed, R. J., Y.-H. Kuo, and S. Low-Nam, 1994: An adiabatic simulation of the ERICA IOP 4 storm: An example of quasi-ideal frontal cyclone development. *Mon. Wea. Rev.*, **122**, 2688–2708, https://doi.org/10.1175/1520-0493(1994)122<2688:AASOTE>2.0.CO;2.

Rios-Berrios, R., R. D. Torn, and C. A. Davis, 2016a: An ensemble approach to investigate tropical cyclone intensification in sheared environments. Part I: Katia (2011). *J. Atmos. Sci.*, **73**, 71–93, https://doi.org/10.1175/JAS-D-15-0052.1.

——, ——, and ——, 2016b: An ensemble approach to investigate tropical cyclone intensification in sheared environments. Part II: Ophelia (2011). *J. Atmos. Sci.*, **73**, 1555–1575, https://doi.org/10.1175/JAS-D-15-0245.1.

——, C. A. Davis, and R. D. Torn, 2018: A hypothesis for the intensification of tropical cyclones under moderate vertical wind shear. *J. Atmos. Sci.*, **75**, 4149–4173, https://doi.org/10.1175/JAS-D-18-0070.1.

Rotunno, R., and J. B. Klemp, 1985: On the rotation and propagation of simulated supercell thunderstorms. *J. Atmos. Sci.*, **42**, 271–292, https://doi.org/10.1175/1520-0469(1985)042<0271:OTRAPO>2.0.CO;2.

Sanders, F., and J. R. Gyakum, 1980: Synoptic-dynamic climatology of the "bomb." *Mon. Wea. Rev.*, **108**, 1589–1606, https://doi.org/10.1175/1520-0493(1980)108<1589:SDCOT>2.0.CO;2.

Schemm, S., and H. Wernli, 2014: The linkage between the warm and the cold conveyor belts in an idealized extratropical cyclone. *J. Atmos. Sci.*, **71**, 1443–1459, https://doi.org/10.1175/JAS-D-13-0177.1.

Schwartz, C. S., G. S. Romine, R. A. Sobash, K. R. Fossell, and M. L. Weisman, 2019: NCAR's real-time convection-allowing ensemble project. *Bull. Amer. Meteor. Soc.*, **100**, 321–343, https://doi.org/10.1175/BAMS-D-17-0297.1.

Shapiro, M. A., and D. Keyser, 1990: Fronts, jet streams, and the tropopause. *Extratropical Cyclones: The Erik Palmén Memorial Volume*, C. Newton and E. O. Holopainen, Eds., Amer. Meteor. Soc., 167–191.

Skamarock, W. C., and Coauthors, 2008: A description of the Advanced Research WRF version 3. NCAR Tech. Note NCAR/TN-475+STR, 113 pp., https://doi.org/10.5065/D68S4MVH.

Spensberger, C., and S. Schemm, 2020: Front-orography interactions during landfall of the 1992 New Year's Day storm. *Wea. Climate Dyn.*, **1**, 175–189, https://doi.org/10.5194/wcd-1-175-2020.

Takayabu, I., 1986: Roles of the horizontal advection on the formation of surface fronts and on the occlusion of a cyclone developing in the baroclinic westerly jet. *J. Meteor. Soc. Japan*, **64**, 329–345, https://doi.org/10.2151/jmsj1965.64.3_329.

Thorncroft, C. D., B. J. Hoskins, and M. E. McIntyre, 1993: Two paradigms of baroclinic-wave life-cycle behaviour. *Quart. J. Roy. Meteor. Soc.*, **119**, 17–55, https://doi.org/10.1002/qj.49711950903.

Trapp, R. J., and M. L. Weisman, 2003: Low-level mesovortices within squall lines and bow echoes. Part II: Their genesis and implications. *Mon. Wea. Rev.*, **131**, 2804–2823, https://doi.org/10.1175/1520-0493(2003)131<2804:LMWSLA>2.0.CO;2.

Trier, S. B., and C. A. Davis, 2007: Mesoscale convective vortices observed during BAMEX. Part II: Influences on secondary deep convection. *Mon. Wea. Rev.*, **135**, 2051–2075, https://doi.org/10.1175/MWR3399.1.

Wakimoto, R. M., N. T. Atkins, and C. Liu, 1995: Observations of the early evolution of an explosive oceanic cyclone during ERICA IOP 5. Part II: Airborne Doppler analysis of the mesoscale circulation and frontal structure. *Mon. Wea. Rev.*, **123**, 1311–1327, https://doi.org/10.1175/1520-0493(1995)123<1311:OOTEEO>2.0.CO;2.

——, H. V. Murphey, C. A. Davis, and N. T. Atkins, 2006: High winds generated by bow echoes. Part II: The relationship

between the mesovortices and damaging straight-line winds. *Mon. Wea. Rev.*, **134**, 2813–2829, https://doi.org/10.1175/MWR3216.1.

Weisman, M. L., and C. A. Davis, 1998: Mechanisms for the generation of mesoscale vortices within quasi-linear convective systems. *J. Atmos. Sci.*, **55**, 2603–2622, https://doi.org/10.1175/1520-0469(1998)055<2603:MFTGOM>2.0.CO;2.

——, and R. J. Trapp, 2003: Low-level mesovortices within squall lines and bow echoes. Part I: Overview and dependence on environmental shear. *Mon. Wea. Rev.*, **131**, 2779–2803, https://doi.org/10.1175/1520-0493(2003)131<2779:LMWSLA>2.0.CO;2.

——, C. Evans, and L. F. Bosart, 2013: The 8 May 2009 superderecho: Analysis of a real-time explicit convective forecast. *Wea. Forecasting*, **28**, 863–892, https://doi.org/10.1175/WAF-D-12-00023.1.

Wheatley, D. M., and R. Trapp, 2008: The effect of mesoscale heterogeneity on the genesis and structure of mesovortices within quasi-linear convective systems. *Mon. Wea. Rev.*, **136**, 4220–4241, https://doi.org/10.1175/2008MWR2294.1.

Zhang, D.-L., and R. Harvey, 1995: Enhancement of extratropical cyclogenesis by a mesoscale convective system. *J. Atmos. Sci.*, **52**, 1107–1127, https://doi.org/10.1175/1520-0469(1995)052<1107:EOECBA>2.0.CO;2.